

# Electric-field induced structural transition in vertical $\text{MoTe}_2$ - and $\text{Mo}_{1-x}\text{W}_x\text{Te}_2$ -based resistive memories

Feng Zhang<sup>1,2</sup>, Huairuo Zhang<sup>3,4\*</sup>, Sergiy Krylyuk<sup>3,4</sup>, Cory A. Milligan<sup>1,5</sup>, Yuqi Zhu<sup>1,2</sup>, Dmitry Y. Zemlyanov<sup>1</sup>, Leonid A. Bendersky<sup>4</sup>, Benjamin P. Burton<sup>4</sup>, Albert V. Davydov<sup>4</sup> and Joerg Appenzeller<sup>1,2\*</sup>

**Transition metal dichalcogenides have attracted attention as potential building blocks for various electronic applications due to their atomically thin nature and polymorphism. Here, we report an electric-field-induced structural transition from a 2H semiconducting to a distorted transient structure ( $2\text{H}_d$ ) and orthorhombic  $T_d$  conducting phase in vertical  $2\text{H-MoTe}_2$ - and  $\text{Mo}_{1-x}\text{W}_x\text{Te}_2$ -based resistive random access memory (RRAM) devices. RRAM programming voltages are tunable by the transition metal dichalcogenide thickness and show a distinctive trend of requiring lower electric fields for  $\text{Mo}_{1-x}\text{W}_x\text{Te}_2$  alloys versus  $\text{MoTe}_2$  compounds. Devices showed reproducible resistive switching within 10 ns between a high resistive state and a low resistive state. Moreover, using an  $\text{Al}_2\text{O}_3/\text{MoTe}_2$  stack, On/off current ratios of  $10^6$  with programming currents lower than  $1\mu\text{A}$  were achieved in a selectorless RRAM architecture. The sum of these findings demonstrates that controlled electrical state switching in two-dimensional materials is achievable and highlights the potential of transition metal dichalcogenides for memory applications.**

Many applications, such as memristors<sup>1</sup>, micro-motors<sup>2</sup>, electronic oscillators<sup>3</sup> and sensors<sup>4</sup>, greatly benefit from recent trends in the area of ‘phase engineering’. The most prominent materials that are explored in this context are  $\text{VO}_2$  and  $\text{NbO}_2$ , which can both undergo a Mott metal-to-insulator transition<sup>5</sup>, and amorphous-to-crystalline phase change materials such as  $\text{Ge}_2\text{Sb}_2\text{Te}_5$  (ref. 6). Recently, transition metal dichalcogenides (TMDs) have attracted considerable attention in the field of two-dimensional (2D) phase engineering due to their polymorphism. TMDs exist in various crystalline phases, which exhibit semiconducting, semimetallic and metallic properties. In some TMD compounds the energy difference between the various phases is rather moderate<sup>7,8</sup>, so several groups are working on phase engineering in TMDs. For example, an in situ 2H to 1T phase transition in  $\text{MoS}_2$  has been introduced by means of electron beam irradiation<sup>9</sup>, and this transition has also been achieved through lithium intercalation<sup>10</sup>. However,  $\text{MoS}_2$  might not be the ideal candidate for TMD phase engineering. Because it has the lowest energy difference between the 2H and 1T’ phases among all TMDs<sup>7,8</sup>,  $\text{MoTe}_2$  appears to be the most promising compound for phase change applications. Experimental results for  $\text{MoTe}_2$  include a strain-induced semiconductor-to-metal transition<sup>11</sup> and growth-controlled stabilization of different  $\text{MoTe}_2$  phases by choosing a specific substrate<sup>12</sup> and through manipulation of the tellurization rate<sup>13</sup> and growth temperature<sup>14–16</sup>. So far, the closest to a demonstration of electrically assisted phase change switching is a 2H to 1T’ transformation in monolayer  $\text{MoTe}_2$  induced by electrostatic liquid gating<sup>17</sup>, albeit without fabricating two-terminal electrical devices to utilize the semiconductor–metal transition. Therefore, device-compatible

methods to enable reversible switching between the different crystalline phases in  $\text{MoTe}_2$  have yet to be reported.

Ultimately, for device applications, controlling the crystal structure of a TMD compound with an electric field and introducing a reproducible phase transition between two distinctly different resistive states is most desirable. Here, we experimentally demonstrate an electric-field-induced reversible structural transition in vertical devices made of  $\text{MoTe}_2$  and  $\text{Mo}_{1-x}\text{W}_x\text{Te}_2$  layers sandwiched between metal or graphene electrodes. A combination of electrical measurements with scanning transmission electron microscopy (STEM) revealed the formation of a conductive filament in the TMD layer, made of a transient structure (named  $2\text{H}_d$ ) that can be viewed as a distorted 2H state, after applying an electrical field. Temperature-dependent measurements further confirmed that the newly formed  $2\text{H}_d$  structure exhibits electrical properties that range from semiconducting to metallic, with devices showing temperature trends that are consistent with a metallic behaviour for the lowest observed resistance values, indicating that the  $2\text{H}_d$  state is a transient state between the semiconducting 2H phase and the metallic 1T’ or  $T_d$  phase.

## 2H- $\text{MoTe}_2$ - and 2H- $\text{Mo}_{1-x}\text{W}_x\text{Te}_2$ -based RRAM

Figure 1a shows a schematic as well as optical microscopy and SEM images of a typical vertical TMD resistive random access memory (RRAM) device under investigation. The top contact area is  $\sim 0.1\mu\text{m}^2$ . Our device design ensures that only vertical transport occurs between the two electrodes, with no lateral transport contribution. Because of the large aspect ratio between the top contact area and the flake thickness, spreading resistance contributions can be

<sup>1</sup>Birck Nanotechnology Center, Purdue University, West Lafayette, IN, USA. <sup>2</sup>Department of Electrical and Computer Engineering, Purdue University, West Lafayette, IN, USA. <sup>3</sup>Theiss Research, Inc., La Jolla, CA, USA. <sup>4</sup>Materials Science and Engineering Division, National Institute of Standards and Technology (NIST), Gaithersburg, MD, USA. <sup>5</sup>School of Chemical Engineering, Purdue University, West Lafayette, IN, USA.

\*e-mail: [huairuo.zhang@nist.gov](mailto:huairuo.zhang@nist.gov); [appenzeller@purdue.edu](mailto:appenzeller@purdue.edu)

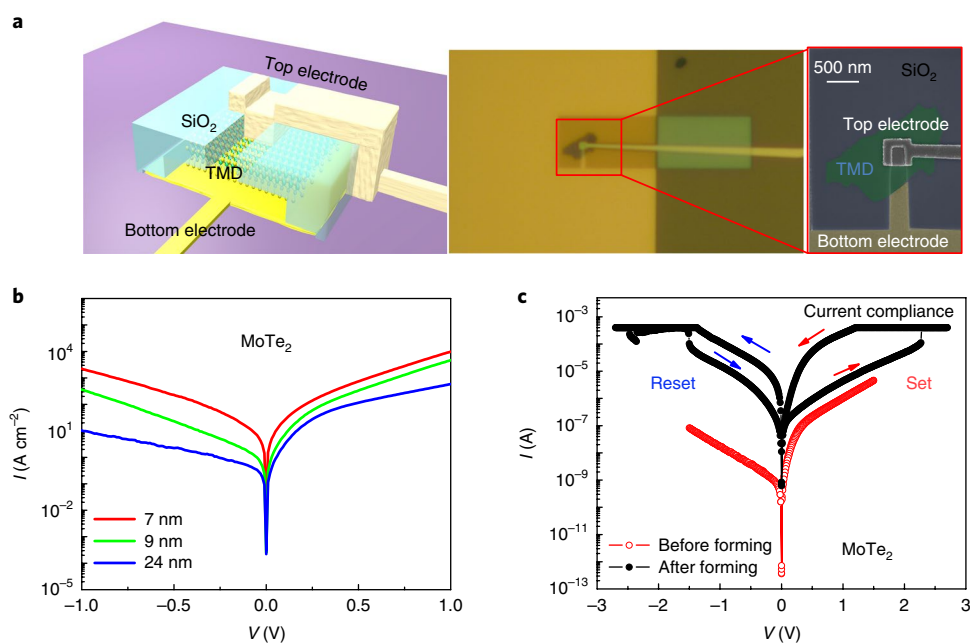


**Fig. 1 | Vertical TMD-based device characterization.** **a**, Schematic diagram of a vertical TMD device and optical and SEM images showing the top (Ti/Ni) and bottom (Ti/Au) electrodes and the SiO<sub>2</sub> isolation layer as well as the actual flake. **b**, Area-normalized  $I$ - $V$  curves of vertical MoTe<sub>2</sub> devices before electroforming for different flake thicknesses. **c**,  $I$ - $V$  curves of a vertical MoTe<sub>2</sub> device from a flake with a thickness of 24 nm and a contact area of 520 nm × 330 nm. Red circles show  $I$ - $V$  curves before memristive switching. Filled black dots show the current versus voltage dependence after forming. Arrows indicate the sweep direction of the applied d.c. voltage. The current compliance is set to 400 μA.

ignored and the active device area is defined by the top contact area. Area-normalized  $I$ - $V$  curves of exemplary vertical MoTe<sub>2</sub> devices are shown in Fig. 1b. For all measurements the bottom electrode was grounded. Experimental current densities follow the expected trend with thickness. Device characteristics are reproducible and do not change substantially after multiple scans between  $-1$  V and  $+1$  V.

The situation changes when the voltage range is extended. MoTe<sub>2</sub> devices can transition into a low resistive state (LRS), as illustrated in Fig. 1c, at a set voltage (here  $V_{\text{set}} = 2.3$  V). Details about the forming process are provided in the Supplementary Information. After the forming event, the device characteristics can be cycled to exhibit typical bipolar RRAM behaviour. Note that, after the forming has occurred, the high resistive state (HRS) always remains more conductive than the original state of the device, indicating that a permanent electronic change has occurred. For the case shown in Fig. 1c, the current ratio between the HRS and the LRS is  $\sim 50$  at  $V_{\text{read}} = 1$  V when the compliance is set to 400 μA.

To further explore the switching mechanism in TMDs, RRAM cells with exfoliated MoTe<sub>2</sub> layer thicknesses between 6 nm and 36 nm were fabricated. All cells were non-volatile and stable (see Supplementary Fig. 2b for read disturb measurements). Before the forming process, the current per unit area through the vertical structures scales in an approximately inversely proportional manner with the flake thickness for not too small voltages (Fig. 1b). However, once the system transitions into its LRS, the current levels (below compliance) are rather similar and do not show any coherent scaling trend with the flake thickness or active device area. This observation is consistent with the notion that the formation of the conductive filaments that enable the LRS is not uniform but gives rise to local current paths. For flake thicknesses from 6 nm to 36 nm, the set voltages can be tuned from 0.9 V to 2.3 V (Fig. 2d). It is noteworthy that the RRAM behaviour is independent of the contact metal used, which indicates that the switching mechanism does not

involve tunnelling through the interfacial Schottky barriers or metal ion diffusion. For example, employing Ni or graphene instead of Ti/Ni as the top electrode resulted in the same RRAM performance as reported here. In addition, a compositional energy-dispersive X-ray spectroscopy (EDS) line scan analysis through the filament area in the Ti/MoTe<sub>2</sub>/Au cross-section STEM sample shows that metal ion diffusion is not the reason for the observed RRAM behaviour in MoTe<sub>2</sub> devices (Supplementary Section 3).

Next, we explored the impact of the material preparation and composition on the RRAM characteristics by extending the experiments to 2H-MoTe<sub>2</sub> samples obtained using different synthesis approaches, and also to 2H-Mo<sub>1-x</sub>W<sub>x</sub>Te<sub>2</sub> alloys. The similar switching characteristics seen in MoTe<sub>2</sub> devices fabricated using either commercially obtained material or single crystals synthesized in this work by chemical vapour transport indicate that the observed RRAM effect does not depend on the material processing conditions. Mo<sub>1-x</sub>W<sub>x</sub>Te<sub>2</sub> devices exhibit very similar switching behaviour, and their set voltages also depend monotonically on the flake thickness (Fig. 2c,d). It is noteworthy that, although we are currently unable to resolve a quantitative trend of the set voltages as a function of composition  $x$  in Mo<sub>1-x</sub>W<sub>x</sub>Te<sub>2</sub> alloys, the set voltages for the Mo<sub>1-x</sub>W<sub>x</sub>Te<sub>2</sub> devices show a tendency of being smaller than the set voltages of the MoTe<sub>2</sub> devices. This implies that the critical electric field needed to trigger the RRAM behaviour may have been reduced in the alloys. Density functional theory (DFT) calculations<sup>8,18,19</sup> and recent experimental results<sup>20,21</sup> indicate that the energy required to transform the semiconducting state into the metallic state is increasingly lower in Mo<sub>1-x</sub>W<sub>x</sub>Te<sub>2</sub> alloys with increasing  $x$ , which in turn should reduce the set voltage in Mo<sub>1-x</sub>W<sub>x</sub>Te<sub>2</sub> devices as compared to their MoTe<sub>2</sub> counterpart. Figure 2d shows experimental evidence of this trend.

### Electric-field induced 2H to 2H<sub>d</sub> transition

In general, the electroforming process in RRAM devices aims at creating a conductive filament by applying a sufficiently high electrical

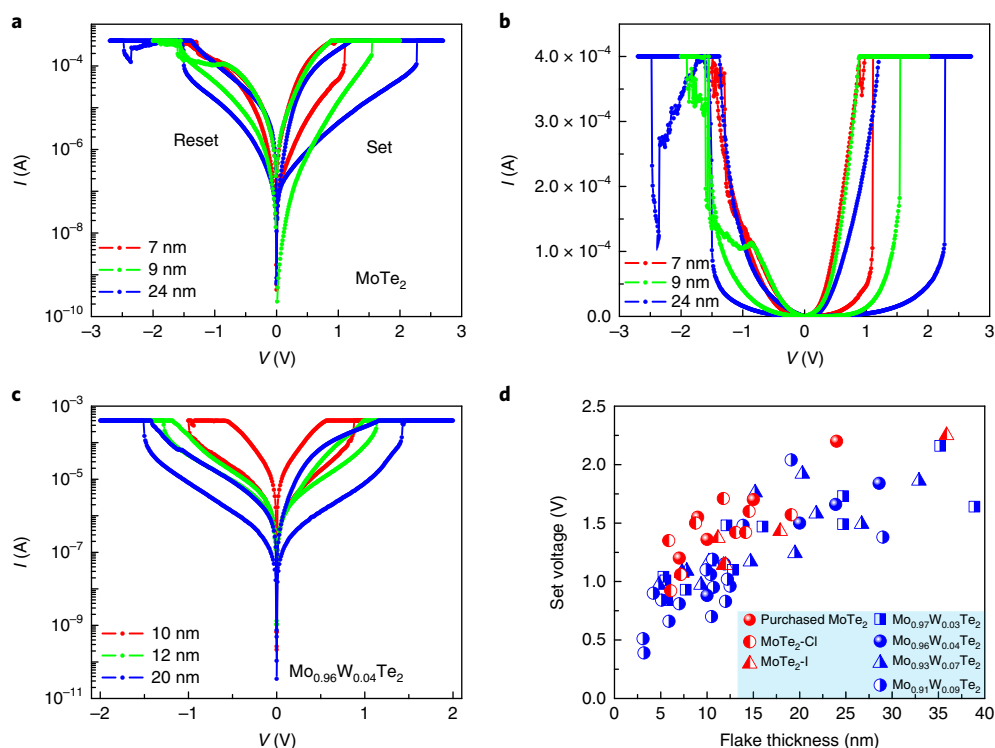


**Fig. 2 | 2H-MoTe<sub>2</sub>- and 2H-Mo<sub>1-x</sub>W<sub>x</sub>Te<sub>2</sub>-based RRAM behaviour and their set voltages as a function of flake thickness. **a, b**, Log (**a**) and linear (**b**) scale *I*-*V* curves of vertical MoTe<sub>2</sub> RRAM devices after electroforming. The active device areas of the 7, 9 and 24 nm MoTe<sub>2</sub> flake devices are 542 nm × 360 nm, 542 nm × 360 nm and 518 nm × 332 nm, respectively. **c**, Log-scale *I*-*V* curves of vertical Mo<sub>0.96</sub>W<sub>0.04</sub>Te<sub>2</sub> RRAM devices after electroforming with a current compliance of 400 μA. The active device area of the 10, 12 and 20 nm Mo<sub>0.96</sub>W<sub>0.04</sub>Te<sub>2</sub> flake devices are 500 nm × 380 nm, 522 nm × 400 nm and 510 nm × 384 nm, respectively. **d**, Set voltage values scale with the flake thickness of MoTe<sub>2</sub>, Mo<sub>0.97</sub>W<sub>0.03</sub>Te<sub>2</sub>, Mo<sub>0.96</sub>W<sub>0.04</sub>Te<sub>2</sub>, Mo<sub>0.93</sub>W<sub>0.07</sub>Te<sub>2</sub> and Mo<sub>0.91</sub>W<sub>0.09</sub>Te<sub>2</sub>. The error bars for the set voltages and the flake thicknesses are in the range of the sizes of the dots. MoTe<sub>2</sub>-Cl and MoTe<sub>2</sub>-I denote crystals grown with TeCl<sub>4</sub> and I<sub>2</sub> transport agents, respectively.**

bias, which in turn results in an electric field and Joule heating inside the sample<sup>22</sup>. The bipolar RRAM behaviour of the MoTe<sub>2</sub> and Mo<sub>1-x</sub>W<sub>x</sub>Te<sub>2</sub> devices shown in Fig. 2 suggests that the main driving force for the switching is the electric field rather than Joule heating (Supplementary Section 4). To confirm the formation of conductive filaments in the case of MoTe<sub>2</sub> RRAM cells, conductive atomic force microscopy (C-AFM) measurements were carried out. First, a fully functional MoTe<sub>2</sub> device was biased to form the LRS, and then the top electrode was removed by wet chemical etching as described in Supplementary Section 14. This approach allows access to the TMD surface after filament formation to perform a local analysis of the surface resistivity after the forming process has occurred. As shown in the inset of Fig. 3a (indicated by an arrow), a bright spot, ~80 nm in diameter, which was formerly covered by the top electrode (red rectangle), is indicative of a higher conductivity path through the TMD layer. For comparison, those MoTe<sub>2</sub> flakes that did not undergo a forming process show a uniform highly resistive surface (Fig. 3b).

To identify the exact nature of the observed filaments, STEM of cross-sectional samples was utilized for both MoTe<sub>2</sub> and Mo<sub>1-x</sub>W<sub>x</sub>Te<sub>2</sub> devices. Before performing the STEM analysis, RRAM devices underwent the same forming process as described above to create conducting filaments in the TMD layers. In total, more than 20 devices were carefully analysed by STEM. Figure 3c shows a high-angle annular dark field (HAADF) STEM image of a Mo<sub>0.96</sub>W<sub>0.04</sub>Te<sub>2</sub> device cross-section. The RRAM structure is clearly visible from the HAADF contrast (which is similar to the MoTe<sub>2</sub> device cross-section shown in Supplementary Fig. 10a,b). Note that the HAADF images display the TMD layer both in the active and

non-active region, where the SiO<sub>2</sub> isolation layer on top of the TMD is preventing RRAM operation. While only the original 2H phase is always observed in the non-active region, two structurally distinct domains can be clearly recognized in the active region; these domains are marked 2H and 2H<sub>d</sub>, respectively, in Fig. 3d, which shows a magnified HAADF image of the red-marked box in Fig. 3c). The 2H<sub>d</sub> region extends vertically throughout the whole TMD layer thickness in this case, but the cross-sectional view often displays the 2H and 2H<sub>d</sub> structures simultaneously (Fig. 4a) when the cut through the device does not perfectly hit the filament core. The 2H<sub>d</sub> region in Fig. 3d is ~80 nm wide and is separated from adjacent 2H regions by boundaries marked as white dash-dotted lines in the figure. The width of the 2H<sub>d</sub> region is consistent with the diameter of the conducting filaments measured by C-AFM. Figure 3e shows an atomic HAADF image in the [110]<sub>2H</sub> zone axis of the 2H region, where well-resolved atomic columns of Mo/W and Te and interlayer van der Waals gaps of the hexagonal 2H structure are clearly visible. Figure 3f shows a structural HAADF image from the 2H<sub>d</sub> domain in the corresponding orientation. Instead of the well-aligned atomic columns of the 2H structure, the atomic columns of the 2H<sub>d</sub> structure are not clearly resolved (note that similar 2H<sub>d</sub> structural features were observed for the MoTe<sub>2</sub> device, as shown in Supplementary Fig. 10).

In an attempt to obtain additional structural information for the 2H<sub>d</sub> structure, the STEM sample was tilted 30° around the *c* axis to the [120]<sub>2H</sub> zone axis. For the 2H structure, Fig. 3g shows the well-resolved atomic columns of this phase. For the 2H<sub>d</sub> structure, Fig. 3h shows ‘smearing’ of the Te and Mo/W atomic columns, displacement along the *c* direction, and preserved interlayer van der

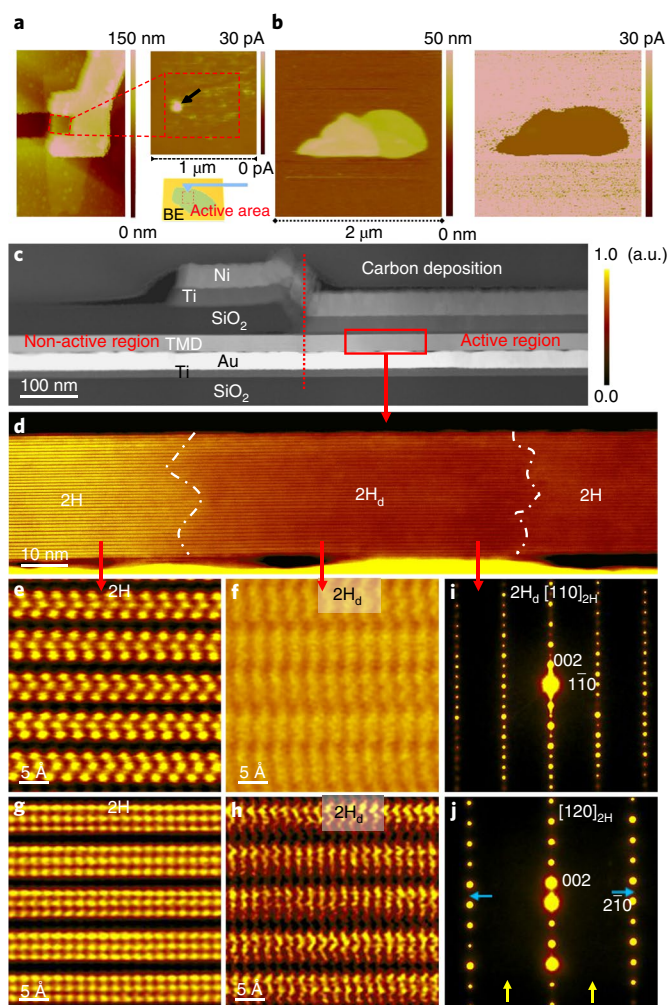


**Fig. 3 | C-AFM and STEM measurements and analysis.** **a**, Current mapping, using C-AFM, of a MoTe<sub>2</sub> flake after the set process and formation of the LRS. Left, topography image of the device before removal of the top electrode. Top-right, current map image after top-electrode wet-etching. The red dashed square denotes the active device area before removal of the top electrode. Note the bright spot marked with an arrow, which we interpret as a filament. Lower-right, experimental set-up schematic. **b**, C-AFM images of a pristine MoTe<sub>2</sub> flake (left, topography; right, current map) showing no indication of the aforementioned highly conductive area. **c**, HAADF-STEM image showing cross-section of the Mo<sub>0.96</sub>W<sub>0.04</sub>Te<sub>2</sub> device. **d**, Higher-magnification HAADF image from the region defined by a red box in **c** and showing coexistence of a distorted structure (2H<sub>d</sub>) with 2H. **e, f, g, h**, Atomic-resolution HAADF images taken along the [110]<sub>2H</sub> zone axis (**e, f**) and [120]<sub>2H</sub> zone axis (**g, h**), showing the intact 2H and distorted 2H<sub>d</sub> structures, respectively. **i, j**, Corresponding nanobeam diffraction pattern taken from the distorted 2H<sub>d</sub> area, which is still indexed as the 2H structure. False colours are added to aid the eye.

Waals gaps. Nanobeam diffraction was performed to determine the crystallography of the 2H<sub>d</sub> structure. Figure 3*i, j* presents nanobeam diffraction patterns taken from the 2H<sub>d</sub> regions in the [110]<sub>2H</sub> and [120]<sub>2H</sub> zone axes, respectively. These diffraction patterns are very similar to the corresponding pattern from the 2H region, which is surprising considering the clear differences in the atomic images of these two regions (Fig. 3*e, f* and 3*g, h*, as well as Supplementary Fig. 10*d-f* for the MoTe<sub>2</sub> case). A detailed analysis of the elemental distribution of Te and Mo in the 2H<sub>d</sub> region (see EDS scan in

Supplementary Fig. 4) shows a similar Mo:Te stoichiometric ratio in the filament and pristine regions. However, due to the limitations in the STEM-EDS line-scan, such as the beam damage and sample/beam drifting issues, the rapidly acquired EDS spectra cannot completely exclude the possibility of vacancies in the filament. Moreover, because the structural images from 2H<sub>d</sub> do not show well-separated atomic columns, and the exact arrangement of atoms in the 2H<sub>d</sub> structure varies from device to device and for different focused ion beam (FIB) cuts, with possible interference from overlapping with the 2H matrix, it is extremely difficult to derive a precise structural model for the 2H<sub>d</sub> structure directly from the HAADF images by relying only on the positions and average composition of the columns (Supplementary Section 9). Instead, we employed a more detailed experimental approach to better understand the observed 2H<sub>d</sub> structure.

Most of the devices studied in the way described above exhibited similar behaviour, with the 2H structure in the matrix and the 2H<sub>d</sub> structure in the filament. However, one device, as shown in Fig. 4*b*, displayed a filament consisting of the 2H phase together with the orthorhombic T<sub>d</sub> phase. This is an unexpected finding, because 1T' MoTe<sub>2</sub> should be more stable than the T<sub>d</sub> phase at room temperature and above (although the T<sub>d</sub> phase can be formed from the 1T' phase at temperatures below ~240 K; ref. 23). This observation, which is substantiated by the fast Fourier transform pattern in the inset of Fig. 4*b* and the matching atomic structure model in Fig. 4*c*, is a clear indication that phases that are typically not stable in a bulk state can be stabilized in a heterostructure due to the particular boundary conditions.

This finding and the fact that we had observed a span of LRS values for different compliance settings and scanning conditions prompted us to perform temperature-dependent electrical measurements. We carefully compared the temperature-dependent electrical properties of the intrinsic 2H phase with the HRS and LRS states, as well as with reference devices fabricated from 1T' MoTe<sub>2</sub>. The test devices were set to the HRS and LRS, respectively, at room temperature, and then characterized as a function of temperature from 160 K to 400 K at a voltage of 0.5 V. Devices kept their original state (either LRS or HRS) during the full temperature cycle. Figure 4*d* shows the result of our temperature-dependent characterization. Both the intrinsic 2H state and the HRS show a distinctly higher resistance at lower temperatures, which is consistent with semiconducting behaviour. On the other hand, for the LRS devices there is a clear spread in the temperature-dependent resistance slopes with a decreasing slope for decreasing sample resistance in the LRS. Interestingly, the lowest resistance values that we observed in the LRS and the corresponding slopes as a function of inverse temperature are approaching what was measured for reference 1T' MoTe<sub>2</sub> samples. Moreover, as shown in Supplementary Section 11, the device with the T<sub>d</sub> phase shown in Fig. 4*b* exhibited the lowest observed resistance values after setting. The sum of these observations in conjunction with the observed 2H<sub>d</sub> structure and T<sub>d</sub> phase from STEM after setting provides experimental evidence that the observed 2H<sub>d</sub> structure is a transitional structural state between 2H and 1T' or T<sub>d</sub> (Supplementary Section 9). Devices that exhibit the lowest LRS values are electrically more similar to the 1T' or T<sub>d</sub> phase, while devices with higher LRS exhibit a transient 2H<sub>d</sub> state.

To explore whether the observed 2H<sub>d</sub> structure is theoretically a (meta)stable new phase, DFT calculations were carried out based on the model proposed in Supplementary Section 9. Preliminary calculations show that the 2H<sub>d</sub> structure is non-stable and relaxes towards the 2H phase (Supplementary Section 10). Note that this finding remains inconclusive, because the boundaries between the different structures as observed in the experiments; Figs. 3*d* and 4*a, b*) that can be expected to drastically impact the energy landscape for the various states in MoTe<sub>2</sub> are not captured in this DFT simulation.

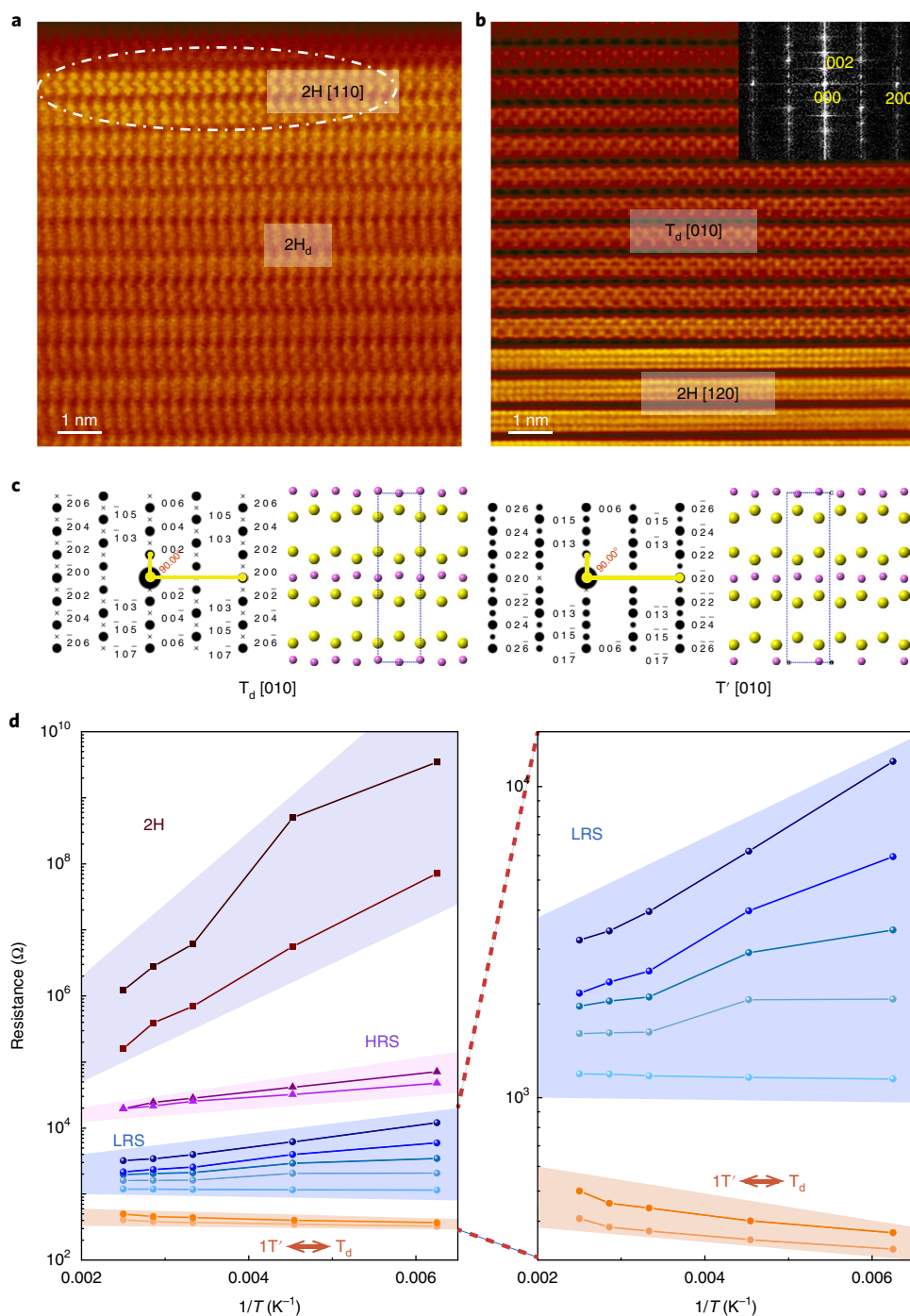


**Fig. 4 | STEM images and resistance of vertical MoTe<sub>2</sub>-based devices versus temperature in their respective 2H phase, HRS, LRS and 1T' phase.** **a**, Atomic-resolution HAADF image taken along the [110]<sub>2H</sub> zone axis from the filament area, showing the coexistence of 2H<sub>d</sub> and 2H regions. **b**, Atomic-resolution HAADF image taken along [120]<sub>2H</sub> zone axis—an orthorhombic T<sub>d</sub> phase is clearly observed together with the 2H phase. Top right inset, Corresponding fast Fourier transform image. **c**, Structural projections of two corresponding variants of orthorhombic T<sub>d</sub> and monoclinic 1T' phases of MoTe<sub>2</sub> (left) and simulated electron diffraction patterns (right). **d**, Semiconducting behaviour is observed for the 2H intrinsic state and for the HRS state. The 1T'/T<sub>d</sub> device at the bottom shows clear metallic behaviour, as is apparent from the decrease in sample resistance towards lower temperatures. The LRS temperature-dependent results show a gradual change in their slope, indicating a transition from semiconducting to metallic behaviour. Note that each line is obtained from an individual device that was set to the corresponding state at room temperature before the temperature-dependent measurements were performed.

Moreover, due to the limitation of the experiments, vacancy diffusion or other effects cannot be completely excluded for the formation of the observed 2H<sub>d</sub> structure. Future studies are needed to investigate all plausible mechanisms.

### 2H-MoTe<sub>2</sub>-based RRAM under pulsed operation

Pulse measurements were used to explore the switching speed to toggle between the two states in MoTe<sub>2</sub>. Figure 5a shows the applied set and reset voltages across the device as a function of time. The set

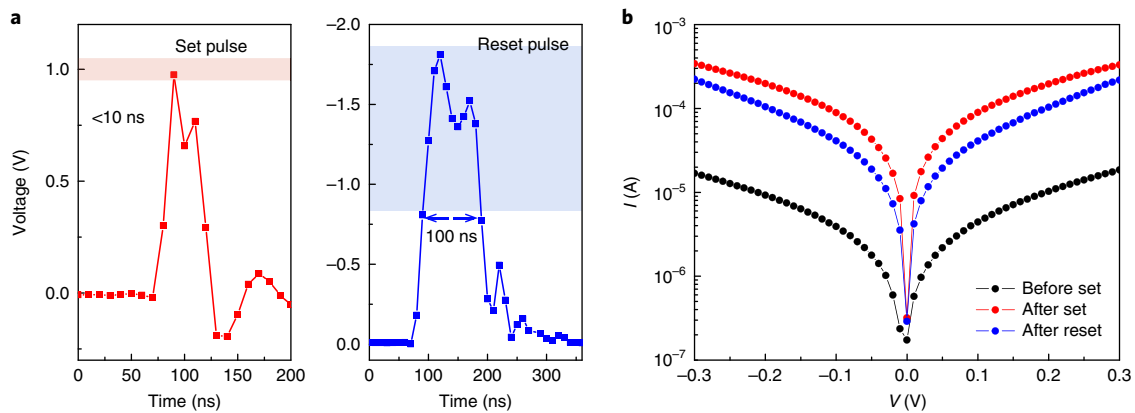


**Fig. 5 | Performance of 2H-MoTe<sub>2</sub>-based RRAM under pulsed operation.** **a**, Device voltage during set/reset operations of a device with 8 nm flake thickness. The set voltage is  $1 \pm 0.1$  V and the effective set pulse width is less than 10 ns. The reset voltage is larger than  $-0.8$  V and the effective reset pulse width is about 100 ns. **b**, Device read current at different states.

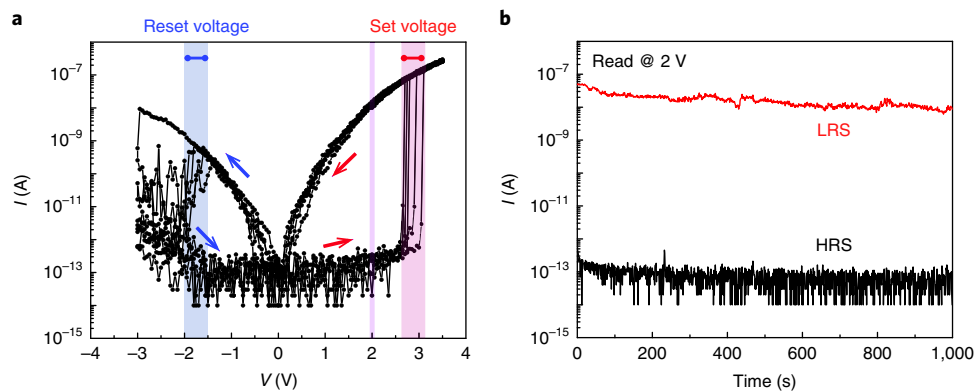


**Fig. 6 | Performance of 2H-Al<sub>2</sub>O<sub>3</sub>/MoTe<sub>2</sub>-based RRAM.** **a**, Multiple  $I$ - $V$  measurements on a vertical metal-Al<sub>2</sub>O<sub>3</sub>/MoTe<sub>2</sub>-metal RRAM cell with a flake thickness of 12 nm and an area of  $360\text{ nm} \times 390\text{ nm}$ . The set voltage is  $-2.9 \pm 0.25$  V (shaded pink) and the reset voltage is  $-1.75 \pm 0.25$  V (shaded blue). A clear memristive behaviour is visible, with the arrows indicating the sweep direction. **b**, Read disturb measurement of the same RRAM cell at 2 V at room temperature (shaded purple in **a**).

voltage of this device is  $1 \pm 0.1$  V (Supplementary Fig. 6), and the effective set pulse width is accordingly smaller than 10 ns. Notice that the uncompensated parasitic capacitance contributions of the set-up did affect the shape of the pulse curve. From Fig. 5b it is apparent that the device resistance changed from the HRS to the LRS after the pulse set operation, and increased again after the reset pulse, in accordance with our expectations. Note that the current compliance settings in the continuous sweep and pulse modes are unavoidably different, resulting in different HRSs before set and after reset in Fig. 5b. This confirms that changing the 2H state into the 2H<sub>d</sub> state can be achieved with appropriate voltage pulses of less than 10 ns. This value only represents an upper bound for the switching time since the experimental set-up did not permit performing faster pulse measurements. The intrinsic switching speed is believed to be even higher than this initial demonstration.

### Al<sub>2</sub>O<sub>3</sub>/MoTe<sub>2</sub>-based low-programming-current RRAMs

For device applications, the LRS resistance should be sufficiently large that the voltage drop across the interconnects is negligible to ensure proper write/read operation. In addition, the current ratio between the LRS and HRS has to be as large as possible to allow the fabrication of sizable memory arrays. In this context the above-mentioned performance specifications are not ideal, and a modified

TMD-based memory cell needs to be developed. To limit the current through the cell, a tunnelling barrier (Al<sub>2</sub>O<sub>3</sub>) was added into the stack.

Figure 6a shows multiple  $I$ - $V$  measurements on an Al<sub>2</sub>O<sub>3</sub>/MoTe<sub>2</sub> RRAM cell, indicating a stable and reproducible memristive switching of this device. Unlike the previously discussed MoTe<sub>2</sub>-only RRAM cells, modified Al<sub>2</sub>O<sub>3</sub>/MoTe<sub>2</sub> stacks immediately transitioned into an LRS when the applied bias reached 2.9 V, without the previously observed electroforming process. Moreover, no current compliance through external circuitry is needed—another desirable feature in RRAM cells. The stability of the RRAM cell is further underlined in Fig. 6b. The extended stack also gave rise to a much larger current ratio between the LRS and HRS of  $10^5$ – $10^6$  as well as nonlinearities ( $I_{\text{Voperation}}/I_{1/2\text{Voperation}}$  based on a  $V/2$  scheme) of  $\sim 100$  for the LRS, and a resistance in the HRS state larger than  $10\text{ T}\Omega$  (limited by our measurement equipment). The latter is critical for reduced static leakage power consumption and allows the maximum RRAM array size to be increased. Moreover, the low current level in the HRS and LRS may eliminate the need for selector devices<sup>24</sup>. All of the above highlights the relevance of this structure for sub- $1\text{ }\mu\text{A}$  programming currents for selectorless RRAM applications.

Notably, Al<sub>2</sub>O<sub>3</sub> is one of the early materials investigated for RRAM applications. However, in our preliminary testing of vertical

Ti/Au/Al<sub>2</sub>O<sub>3</sub>/Ti/Ni device structures, repeated voltage sweeps did not result in any filament formation and instead led to destructive breakdown at voltages in the 1.35 V range (Supplementary Fig. 17). While we cannot entirely exclude the possibility of filament formation in the Al<sub>2</sub>O<sub>3</sub> layer of the Al<sub>2</sub>O<sub>3</sub>/MoTe<sub>2</sub> stack, the electrical data can be qualitatively understood if filaments are only formed in MoTe<sub>2</sub>, but do not reach through the Al<sub>2</sub>O<sub>3</sub> layer, in this way limiting the LRS conductivity to a much lower, more desirable value of ~10 MΩ as compared to the MoTe<sub>2</sub>-only RRAM cells. In fact, the current levels reached in the LRS of the Al<sub>2</sub>O<sub>3</sub>/MoTe<sub>2</sub> RRAM cell are consistent with the maximum current levels achievable before breakdown in the Ti/Au/Al<sub>2</sub>O<sub>3</sub>/Ti/Ni stack.

## Outlook

In this Article, an electric-field-induced reversible transition from the semiconducting 2H to a higher conducting 2H<sub>d</sub> phase in vertical MoTe<sub>2</sub> and Mo<sub>1-x</sub>W<sub>x</sub>Te<sub>2</sub> RRAM devices has been achieved. Cross-sectional STEM confirmed that the 2H<sub>d</sub> state is formed after a set voltage is applied and that this structure can be described as a transient state between the semiconducting 2H and the metallic 1T' or T<sub>d</sub> phase. Temperature-dependent electrical measurements indicate that the 2H<sub>d</sub> state can exhibit semiconducting to metallic behaviour depending on the status of the transient state. T<sub>d</sub> and 2H co-existing phases in MoTe<sub>2</sub> were observed at room temperature. Our work demonstrates the possibility to locally and selectively engineer phase transitions in TMD layers with an electric field, and demonstrates the potential of TMDs for these types of resistive switching applications.

## Online content

Any methods, additional references, Nature Research reporting summaries, source data, statements of data availability and associated accession codes are available at <https://doi.org/10.1038/s41563-018-0234-y>.

Received: 10 September 2017; Accepted: 26 October 2018;  
Published online: 10 December 2018

## References

- Wuttig, M. & Yamada, N. Phase-change materials for rewriteable data storage. *Nat. Mater.* **6**, 824–832 (2007).
- Liu, K. et al. Powerful, multifunctional torsional micromuscles activated by phase transition. *Adv. Mater.* **26**, 1746–1750 (2014).
- Gu, Q., Falk, A., Wu, J., Ouyang, L. & Park, H. Current-driven phase oscillation and domain-wall propagation in W<sub>x</sub>V<sub>1-x</sub>O<sub>2</sub> nanobeams. *Nano Lett.* **7**, 363–366 (2007).
- Strelcov, E., Lilach, Y. & Kolmakov, A. Gas sensor based on metal–insulator transition in VO<sub>2</sub> nanowire thermistor. *Nano Lett.* **9**, 2322–2326 (2009).
- Zhou, Y. & Ramanathan, S. Mott memory and neuromorphic devices. *Proc. IEEE* **103**, 1289–1310 (2015).
- Wong, H. S. P. et al. Phase change memory. *Proc. IEEE* **98**, 2201–2227 (2010).
- Duerloo, K.-A. N., Li, Y. & Reed, E. J. Structural phase transitions in two-dimensional Mo- and W-dichalcogenide monolayers. *Nat. Commun.* **5**, 4214 (2014).
- Duerloo, K.-A. N. & Reed, E. J. Structural phase transitions by design in monolayer alloys. *ACS Nano* **10**, 289–297 (2016).
- Lin, Y.-C., Dumcenco, D. O., Huang, Y.-S. & Suenaga, K. Atomic mechanism of the semiconducting-to-metallic phase transition in single-layered MoS<sub>2</sub>. *Nat. Nanotech.* **9**, 391–396 (2014).
- Py, M. A. & Haering, R. R. Structural destabilization induced by lithium intercalation in MoS<sub>2</sub> and related compounds. *Can. J. Phys.* **61**, 76–84 (1983).
- Song, S. et al. Room temperature semiconductor–metal transition of MoTe<sub>2</sub> thin films engineered by strain. *Nano Lett.* **16**, 188–193 (2016).
- Tsipas, P. et al. Direct observation at room temperature of the orthorhombic weyl semimetal phase in thin epitaxial MoTe<sub>2</sub>. *Adv. Funct. Mater.* **28**, 1802084 (2018).
- Park, J. C. et al. Phase-engineered synthesis of centimeter-scale 1T' and 2H-molybdenum ditelluride thin films. *ACS Nano* **9**, 6548–6554 (2015).
- Vellinga, M. B., de Jonge, R. & Haas, C. Semiconductor to metal transition in MoTe<sub>2</sub>. *J. Solid State Chem.* **2**, 299–302 (1970).
- Keum, D. H. et al. Bandgap opening in few-layered monoclinic MoTe<sub>2</sub>. *Nat. Phys.* **11**, 482–486 (2015).
- Empante, T. A. et al. Chemical vapor deposition growth of few-layer MoTe<sub>2</sub> in the 2H, 1T' and 1T phases: tunable properties of MoTe<sub>2</sub> films. *ACS Nano* **11**, 900–905 (2017).
- Wang, Y. et al. Structural phase transition in monolayer MoTe<sub>2</sub> driven by electrostatic doping. *Nature* **550**, 487–491 (2017).
- Li, Y., Duerloo, K. A., Wauson, K. & Reed, E. J. Structural semiconductor-to-semimetal phase transition in two-dimensional materials induced by electrostatic gating. *Nat. Commun.* **7**, 10671 (2016).
- Zhang, C. et al. Charge mediated reversible metal–insulator transition in monolayer MoTe<sub>2</sub> and W<sub>x</sub>Mo<sub>1-x</sub>Te<sub>2</sub> alloy. *ACS Nano* **10**, 7370–7375 (2016).
- Sean, M. O. et al. The structural phases and vibrational properties of Mo<sub>1-x</sub>W<sub>x</sub>Te<sub>2</sub> alloys. *2D Mater.* **4**, 045008 (2017).
- lv, Y.-Y. et al. Composition and temperature-dependent phase transition in miscible Mo<sub>1-x</sub>W<sub>x</sub>Te<sub>2</sub> single crystals. *Sci. Rep.* **7**, 44587 (2017).
- Wong, H. S. P. et al. Metal-oxide RRAM. *Proc. IEEE* **100**, 1951–1970 (2012).
- Berger, A. N. et al. Temperature-driven topological transition in 1T'-MoTe<sub>2</sub>. *NPJ Quantum Mater.* **3**, 2 (2018).
- Liang, J. & Wong, H. S. P. Cross-point memory array without cell selectors—device characteristics and data storage pattern dependencies. *IEEE Trans. Electron. Dev.* **57**, 2531–2538 (2010).

## Acknowledgements

This work was supported in part by the Semiconductor Research Corporation (SRC) at the NEWLIMTS Center and National Institute of Standards and Technology (NIST) through award no. 70NANB17H041. S.K. acknowledges support from the US Department of Commerce, NIST under financial assistance award 70NANB16H043. H.Z. acknowledges support from the US Department of Commerce, NIST under financial assistance awards 70NANB15H025 and 70NANB17H249. A.V.D., S.K. and B.P.B. acknowledge support from Material Genome Initiative funding allocated to NIST. The authors thank I. Kalish (NIST) for conducting XRD and EDS measurements on Mo<sub>1-x</sub>W<sub>x</sub>Te<sub>2</sub> samples. Certain commercial equipment, instruments or materials are identified in this paper to specify the experimental procedure adequately. Such identification is not intended to imply recommendation or endorsement by NIST, nor is it intended to imply that the materials or equipment identified are necessarily the best available for the purpose.

## Author contributions

E.Z. and J.A. designed the experiments. E.Z. fabricated, measured the devices and performed the conductive AFM measurement. S.K. and A.V.D. synthesized Mo<sub>1-x</sub>W<sub>x</sub>Te<sub>2</sub> alloy samples. C.A.M. and D.Y.Z. performed the STM and STS measurements. D.Y.Z. contributed the STM surface analysis. H.Z. prepared TEM samples using SEM/FIB and performed TEM/STEM measurements. H.Z., L.A.B. and A.V.D. performed the TEM/STEM analysis. B.P.B. conducted ab initio modelling of energetics for the 2H, 2H<sub>d</sub> and 1T' MoTe<sub>2</sub>. Y.Z. and J.A. carried out the model simulation for vertical electrical transport. E.Z., H.Z., L.A.B., A.V.D. and J.A. wrote the manuscript and discussed the results at all stages.

## Competing interests

The authors declare no competing interests.

## Additional information

Supplementary information is available for this paper at <https://doi.org/10.1038/s41563-018-0234-y>.

Reprints and permissions information is available at [www.nature.com/reprints](http://www.nature.com/reprints).

Correspondence and requests for materials should be addressed to H.Z. or J.A.

Publisher's note: Springer Nature remains neutral with regard to jurisdictional claims in published maps and institutional affiliations.

© This is a U.S. government work and not under copyright protection in the U.S.; foreign copyright protection may apply 2018

## Methods

**Device fabrication and electrical measurements.** A layer of Ti/Au (10 nm/25 nm; acting as a bottom electrode) was deposited onto a 90 nm silicon dioxide ( $\text{SiO}_2$ ) layer located on top of a highly doped silicon wafer. Next, TMD flakes from either  $\text{MoTe}_2$  (2D Semiconductors and NIST) or  $\text{Mo}_{1-x}\text{W}_x\text{Te}_2$  (NIST) were exfoliated onto this electrode using a standard scotch tape technique, followed by thermal evaporation of 55 nm  $\text{SiO}_2$  (acting as an insulating layer). Device fabrication was completed by depositing a Ti/Ni (35 nm/50 nm) top electrode. For Ti/Au/ $\text{Al}_2\text{O}_3$ / $\text{MoTe}_2$ /Ti/Ni vertical devices, a 3-nm-thick Al layer was deposited onto the bottom electrode before its oxidation in an oxygen-rich environment at 250 °C for 6 h. This process formed a 4.5-nm-thick  $\text{Al}_2\text{O}_3$  layer.  $\text{MoTe}_2$  flakes were then peeled onto the  $\text{Al}_2\text{O}_3$ -covered bottom electrodes. The isolation and top electrode formation were identical to the original process flow discussed above for vertical TMD RRAM devices.

Electrical characterization of the devices was performed at room temperature using a parameter analyser (Agilent 4156C). A Keysight B1500A semiconductor device analyser was used for switching speed measurements.

**TMD synthesis and characterization.** Both 1T' and 2H- $\text{Mo}_{1-x}\text{W}_x\text{Te}_2$  crystals ( $x = 0, 0.03, 0.04, 0.07$  and  $0.09$ , where  $x$  is the atomic fraction of W) were produced at NIST using the chemical vapour transport method. First, polycrystalline  $\text{Mo}_{1-x}\text{W}_x\text{Te}_2$  powders were synthesized by reacting stoichiometric amounts of Mo (99.999%), W (99.9%) and Te (99.9%) at 750 °C in a vacuum-sealed quartz ampoule. Next,  $\text{Mo}_{1-x}\text{W}_x\text{Te}_2$  crystals were grown at 950–1,000 °C using ~1 g of poly- $\text{Mo}_{1-x}\text{W}_x\text{Te}_2$  charge and a small amount of I (99.8%, 5 mg cm<sup>-3</sup>) sealed in evacuated quartz ampoules. The ampoules were ice-water-quenched after 7 days of growth, yielding  $\text{Mo}_{1-x}\text{W}_x\text{Te}_2$  crystals in the metallic 1T' phase. The 1T'- $\text{Mo}_{1-x}\text{W}_x\text{Te}_2$  alloy crystals were then converted to the semiconducting 2H phase by annealing in vacuum-sealed ampoules at 950 °C for 24 h (or at 750 °C for 72 h) followed by cooling to room temperature at a 10 °C h<sup>-1</sup> rate. 2H- $\text{MoTe}_2$  crystals were also obtained by chemical vapour transport growth at 800 °C for 140 h using  $\text{TeCl}_4$  (99.9%, 5.7 mg cm<sup>-3</sup>) as a vapour transport agent. At this temperature, which, in

accordance with the Mo-Te phase diagram<sup>25</sup> is below the 1T' → 2H phase transition temperature,  $\text{MoTe}_2$  crystals grow directly in the 2H phase.

The crystal structure and composition of the  $\text{Mo}_{1-x}\text{W}_x\text{Te}_2$  samples were determined by powder X-ray diffraction and energy-dispersive X-ray spectroscopy in SEM, respectively. More detailed information on crystal preparation and characterization can be found in ref. <sup>20</sup>.

**Conductive AFM measurement.** C-AFM was performed in a Veeco Dimension 3100 AFM system. All AFM images were taken in contact mode using SCM-PIT tips (Bruker). The conductive tip consisted of 0.01–0.025 Ω cm antimony-doped Si coated with PtIr.

**TEM/STEM structural characterization.** An FEI Nova NanoLab 600 DualBeam (SEM/FIB) system was used to prepare cross-sectional TEM samples. Electron-beam-induced deposition of 1-μm-thick carbon was initially deposited on top of the device to protect the sample surface, followed by 2-μm ion-beam induced Pt deposition. To reduce Ga ion damage, in the final step of preparation the TEM samples were thinned with 2 kV Ga ions using a low beam current of 29 pA and a small incident angle of 3°. An FEI Titan 80–300 probe-corrected STEM/TEM microscope operating at 300 keV was used to acquire both nanobeam diffraction patterns and TEM images in TEM mode as well as atomic-resolution high-angle annular dark field (HAADF) images in STEM mode.

## Data availability

The data that support the plots within this paper are available from the corresponding author upon request.

## References

25. Brewer, L. & Lamoreaux, R. H. in *Binary Alloy Phase Diagrams* 2nd edn, Vol. 3 (eds. Massalski, T. B., Okamoto, H., Subramanian, P. R. & Kacprzak, L.) 2675–2676 (ASM International, Russell Township, 1990).

In the format provided by the authors and unedited.

# Electric-field induced structural transition in vertical $\text{MoTe}_2$ - and $\text{Mo}_{1-x}\text{W}_x\text{Te}_2$ -based resistive memories

Feng Zhang<sup>1,2</sup>, Huairuo Zhang <sup>3,4\*</sup>, Sergiy Krylyuk<sup>3,4</sup>, Cory A. Milligan<sup>1,5</sup>, Yuqi Zhu<sup>1,2</sup>, Dmitry Y. Zemlyanov<sup>1</sup>, Leonid A. Bendersky<sup>4</sup>, Benjamin P. Burton<sup>4</sup>, Albert V. Davydov<sup>4</sup> and Joerg Appenzeller <sup>1,2\*</sup>

---

<sup>1</sup>Birck Nanotechnology Center, Purdue University, West Lafayette, IN, USA. <sup>2</sup>Department of Electrical and Computer Engineering, Purdue University, West Lafayette, IN, USA. <sup>3</sup>Theiss Research, Inc., La Jolla, CA, USA. <sup>4</sup>Materials Science and Engineering Division, National Institute of Standards and Technology (NIST), Gaithersburg, MD, USA. <sup>5</sup>School of Chemical Engineering, Purdue University, West Lafayette, IN, USA.

\*e-mail: [huairuo.zhang@nist.gov](mailto:huairuo.zhang@nist.gov); [appenzeller@purdue.edu](mailto:appenzeller@purdue.edu)

## Supplementary Information for

### **Electric field induced structural transition in vertical MoTe<sub>2</sub> and Mo<sub>1-x</sub>W<sub>x</sub>Te<sub>2</sub> based resistive memories**

Feng Zhang<sup>1,2</sup>, Huairuo Zhang<sup>3,4\*</sup>, Sergiy Krylyuk<sup>3,4</sup>, Cory A. Milligan<sup>1,5</sup>, Yuqi Zhu<sup>1,2</sup>, Dmitry Y. Zemlyanov<sup>1</sup>, Leonid A. Bendersky<sup>4</sup>, Benjamin P. Burton<sup>4</sup>, Albert V. Davydov<sup>4</sup> and Joerg Appenzeller<sup>1,2\*</sup>

<sup>1</sup>Birck Nanotechnology Center, Purdue University, West Lafayette, Indiana 47907, USA.

<sup>2</sup>Department of Electrical and Computer Engineering, Purdue University, West Lafayette, Indiana 47907, USA.

<sup>3</sup>Theiss Research, Inc., La Jolla, California 92037, USA.

<sup>4</sup>Materials Science and Engineering Division, National Institute of Standards and Technology (NIST), Gaithersburg, Maryland 20899, USA.

<sup>5</sup>School of Chemical Engineering, Purdue University, West Lafayette, Indiana 47907, USA.

\***Corresponding Authors:** appenzeller@purdue.edu (J.A.); huairuo.zhang@nist.gov (H.Z.)

#### **This PDF file includes:**

Supplementary Text

Figs. S1 to S17

## Supplementary Text

### Section S1: MoTe<sub>2</sub> based RRAM electroforming process

Pristine metal-MoTe<sub>2</sub>-metal devices exhibit reproducible I-V curves shown as pink dotted line in Fig. S1(a) and (b) as long as a critical, TMD thickness dependent forming voltage is not reached. Measuring beyond this forming voltage results in the RRAM behavior as described in the main text, triggering the resistive switching behavior. Once a filament is formed, a set voltage lower than the forming voltage is used to switch between the HRS and LRS of the cell. When a reverse polarity electric field is applied, rupture of filaments causes the back transition to the HRS. Note that the set voltage has approximately a linear dependence on the flake thickness for not too thick layers (see Fig. 2(d)) indicating that a critical electric field is needed to trigger the memristive behavior. Cycling the MoTe<sub>2</sub>-based RRAM cells multiple times as shown in Fig. S1(b) results in similar and stable performance specs with set voltages varying by about 0.2 V.

### Section S2: Current compliance setting effect on RRAM performance

For a metal oxide based RRAM cell, the LRS resistance can be controlled by the set current compliance which in turn determines the diameter and/or the number of conductive filaments formed, and the HRS resistance can be changed by the reset voltage through the modulation of the ruptured filament length. MoTe<sub>2</sub>-based RRAM cells, as presented here, show the same behavior as evident from Fig. S2(a). As expected, the higher the current compliance, the lower the LRS resistance becomes. The flake thickness for the device in Fig. S2 is 7 nm. Fig. S2(b) shows the performance of the same device under a 0.5 V read disturb with the current compliance set to 800  $\mu$ A. Both states show a stable resistance value over 1000 s at room temperature.

### Section S3: Impact of the choice of metal electrodes on the RRAM behavior

To date, some preliminary studies have demonstrated memristive behavior in two-terminal TMD-based devices<sup>1-5</sup>. However, these advancements are yet to provide a viable route towards the development of scalable high performance RRAM cells. All of the above instances memristive switching depends on, or is mediated by uncontrollable defects or oxygen vacancies in the active material. In contrast, here we present for the first time vertical bipolar RRAM cells with areas in the 0.1  $\mu$ m<sup>2</sup> range from exfoliated single crystals of MoTe<sub>2</sub> and Mo<sub>1-x</sub>W<sub>x</sub>Te<sub>2</sub> alloys, where the switching is mediated by a controllable 2H to 2H<sub>d</sub> or T<sub>d</sub> transition as shown by various characterization methods in the main text.

In Fig. 1(c), Ti/Ni is used as top contact and Au is utilized as the bottom electrode. In order to understand the role of the metal electrode in the observed RRAM behavior, Ni and graphene are used here to replace the top contact Ti/Ni (where Ti is adjacent to the MoTe<sub>2</sub> film). As apparent from Fig. S3, RRAM behavior is very obvious in both types of devices. This set of experiments thus indicates that the RRAM behavior reported here is independent of the particular metal

contact choice, indicating that the switching mechanism does not involve the interfacial Schottky barriers. More importantly, using graphene, which is known to be an excellent diffusion barrier for metals<sup>6</sup> also results in the same RRAM switching, clearly indicating that the metal electrode and diffusion of metal atoms into the TMD layer does not play a role in the observed switching behavior.

In addition, Fig. S4 shows EDS line-scan results for MoTe<sub>2</sub> based RRAM devices. The devices underwent multiple cycles from the HRS to the LRS. A detailed comparison of the elemental distribution of Te and Mo in the filament and close to the filament regions with the Te to Mo distribution of the pristine structure in the non-active region (Fig.S4(a-d)) suggests almost no change in the Mo:Te stoichiometry. However, the existence of vacancies cannot be entirely ruled out due to the limited resolution of the EDS scans. Moreover, the EDS line scan analysis shows that metal ion diffusion is not the reason for the observed RRAM behavior in MoTe<sub>2</sub> devices. It should be noted that the weak Ti and Au signals detected in the MoTe<sub>2</sub> layer near the Ti/MoTe<sub>2</sub> and MoTe<sub>2</sub>/Au interfaces (Fig. S4(e-h)), arise most likely from sputtering contamination during FIB ion milling, as well as from multi-scattering of a small amount of electrons and X-rays which were re-directed into the neighboring sample area. For example, a Cu signal from the copper TEM sample grid was typically present in the TEM EDS spectrum, as observed in Fig. S4(g-h). Our EDS analysis further supports the above statement that the RRAM behavior is not related to the metal ion diffusion mechanism.

#### Section S4: Bipolar RRAM behavior in MoTe<sub>2</sub> devices

Fig. S5 showing log and linear I-V curves of a 7 nm thick MoTe<sub>2</sub> device, which proves that the MoTe<sub>2</sub> and Mo<sub>x</sub>W<sub>1-x</sub>Te<sub>2</sub> based RRAM devices *are not* unipolar and Joule heating *does not* have a significant impact on the RESET processes. The numbers in the figures are the scanning sequences. First, 0 - 1.2 V is applied to SET the device to the LRS (1), then the scan direction is reversed back (2). Next, the voltage is swept from 0 – 2V (3) and back (4). The device keeps its LRS and remains almost unchanged. Next, the polarity of the voltage is reversed and a scan from 0 – (-1.2) V is performed (5), and back (6), RESETTING the device to its HRS. Therefore, we conclude that the main driving force for the bipolar switching is the electric field, rather than Joule heating.

#### Section S5: Performance of 2H-MoTe<sub>2</sub> based RRAM under pulsed operation

Fig. S6 shows the I-V curve of the device used for the high switching speed measurement displayed in Fig. 5(a) and (b) of the main text. An 8 nm MoTe<sub>2</sub> device with a set voltage of ~1 V and a set voltage variation of about ±0.1 V is employed. A Keysight B1500A semiconductor device analyzer was used to generate the pulse with a minimum (i.e. tool limited) width of 10 ns. The voltage applied on the device was affected by the parasitic capacitance contributions of the measurement set-up, and the effective set voltage width is less than 10 ns as shown in Fig. 5(a) in the main text. Note that there are different current compliance settings in the pulse measurement

(400  $\mu$ A and 1 mA) compared to the continuous sweep mode, resulting in slightly different LRS resistance values for these two modes of measurement, since the current compliance determines the diameter and/or the number of conductive filaments formed as discussed in Section S2.

### Section S6: Electrical characterization of the $\text{Mo}_{0.96}\text{W}_{0.04}\text{Te}_2$ alloy

Fig. S7 displays a typical transfer characteristic of a 2H- $\text{Mo}_{0.96}\text{W}_{0.04}\text{Te}_2$  field effect transistor (FET), indicating that the ternary compound shows clear semiconducting behavior with device characteristics similar to the case of  $\text{MoTe}_2$ .

### Section S7: $\text{MoTe}_2/\text{Mo}_{0.96}\text{W}_{0.04}\text{Te}_2$ switching mechanism exploration by STM and STS

In order to explore the filament formation mechanism further, STM was used to perform a detailed surface analysis at room temperature. 2H- $\text{MoTe}_2$  and 2H-  $\text{Mo}_{0.96}\text{W}_{0.04}\text{Te}_2$  layers were exfoliated from a 2H- $\text{MoTe}_2$  and 2H-  $\text{Mo}_{0.96}\text{W}_{0.04}\text{Te}_2$  bulk crystals (2D Semiconductors and NIST respectively) onto Au pads using standard scotch tape techniques. An Omicron ultrahigh-vacuum (UHV) STM was used to perform the surface analysis of  $\text{MoTe}_2$  and  $\text{Mo}_{0.96}\text{W}_{0.04}\text{Te}_2$  at room temperature. During all measurements, the electrochemically etched tungsten tip was grounded and the voltage was applied to the Au pad. All STM images were recorded at a tunneling current of 2 nA and a bias voltage of -0.9 V. The STM data were analyzed with WSxM software<sup>7</sup>.

Fig. S8 (a) shows a representative STM image of the pristine exfoliated  $\text{MoTe}_2$  flake. The atomic surface structure of the 2H-phase of the  $\text{MoTe}_2$  single crystal demonstrates the expected  $C_3$  symmetry with an interatomic distance of 0.34 nm. Imaging was performed with a bias voltage of -0.9 V. To mimic the situation in  $\text{MoTe}_2$  RRAM cells under forming conditions, a bias of -3 V was applied to a contact underneath the TMD relative to the STM tip while scanning. Next, an STM image was taken again at a bias of -0.9 V. As apparent from Fig. S8 (b) the surface image appears drastically different after voltage application, and non-uniform bright regions are clearly visible in the figure. ‘Protrusions’ with a height of 0.3 nm to 0.6 nm on the sample surface are clearly observed, which are interpreted as possible topographic changes in conjunction with changes in the local density of states (LDOS) (see discussion below). Next, scanning tunneling spectroscopy (STS) measurements were performed at four distinct locations as marked by the colored squares 1 through 4 in Fig. S8 (b). Locations 1 and 2 fall into the region of alteration, while 3 and 4 are located in the unperturbed region of the sample that we will label as “pristine” in the following discussion. Fig. S8 (c) shows the obtained I-V characteristics at the four locations. Higher current levels in particular for small applied voltages are observed for locations 1 and 2 (the modified areas) if compared with 3 and 4 (pristine areas). The corresponding  $dI/dV$  curves shown in Fig. S8 (d) are a measure of the local density of states (LDOS). While characteristics obtained for the pristine areas (locations 3 and 4) indicate the presence of a sizable bandgap in the range of 0.85 eV, consistent with the extracted bandgap of 2H- $\text{MoTe}_2$  from electrical measurements<sup>8</sup>, the LDOS of locations 1 and 2 shows a finite density of states

even at zero bias, implying that these regions had become metallic or reflect the behavior of a small bandgap semiconductor after a forming voltage had been applied. At a first glance, the positions of atoms in the modified (red circle) and the pristine (green circles) regions occur identical ( $C_3$  symmetry) as shown in the zoom-in Fig. S8 (b). However, by comparing the positions of atomic sites along the red and green dashed lines, a clear distortion between tellurium atoms in the pristine and voltage disturbed areas is apparent. The atomic rows of Te in the pristine and voltage modified areas are rotated relative to each other by  $3^\circ$  to  $6^\circ$  as shown in Fig. S8 (b). The same phenomenon is observed when  $\text{Mo}_{0.96}\text{W}_{0.04}\text{Te}_2$  devices are analyzed by STM. Last, it is important to note that – like in the RRAM cell – features of enhanced conductivity that were created by applying a voltage of  $-3$  V can be turned semiconducting again by applying a voltage of opposite polarity. To demonstrate this behavior, setting and resetting was performed in an in-situ STM experiment. Note that in this measurement set-up the exact value of the set/reset voltage at the flake underneath the STM tip was not known. This is an important statement since  $\text{MoTe}_2$  based RRAM devices **can be set again with too large reset voltages**. Fig. S9 (a) shows an STM image of a  $\text{MoTe}_2$  flake after applying  $-3$  V, while Fig. S9 (b) shows an image after  $+3$  V scanning. In order to compare those two images, the bright spot marked 1 was used as a point of reference. Relative to this point, areas 2 through 5 were marked that showed bright spots in Fig. S9 (a). In Fig. S9 (b) the bright spots 3 and 4 have been changed back to “pristine” (darker) surfaces as expected when applying a reverse voltage. One also notices that portions of the  $\text{MoTe}_2$  lattice adjacent to positions 3 and 4 became bright, which indicates that the voltage of  $+3$  V has had two effects: a) it changed some bright regions back into pristine portions (RESET) and b) altered some pristine parts to become bright (SET) simultaneously.

The above findings are in principle consistent with our observations, reported in the main text, that an electric field induced reversible structural transition is achievable in  $\text{MoTe}_2$  and  $\text{Mo}_{1-x}\text{W}_x\text{Te}_2$ . However, the STM and STS data presented here may not perfectly correlate to the RRAM behavior reported in the main text due to the different boundary conditions, for example, the presence vs. absence of a top electrode covering the surface. Moreover, it should be noted that the STM experiment can only characterize the  $\text{MoTe}_2$  surface rather than the whole layer of frequently tens of nanometers in thickness.

The sum of these observations leads us to believe that  $\text{MoTe}_2$  undergoes a reversible structural transition from a semiconducting to a higher conductive state under application of an electric field, which is responsible for the RRAM behavior observed by us and reported in the main text.

### Section S8: STEM analysis

The same  $2H$  to  $2H_d$  structural transition discussed in the context of Fig. 3 in the main text for the  $\text{Mo}_{0.96}\text{W}_{0.04}\text{Te}_2$  device was also observed in  $\text{MoTe}_2$  based devices. Fig. S10 (a) shows a low-magnification bright-field transmission electron microscopy (TEM) image of a  $\text{MoTe}_2$  device cross-section. In the image two regions can be identified: Area 1, which corresponds to the

original 2H structure outside of the active electrical contact, and Area 2, which corresponds to the electrically cycled part of the device. Fig. S10 (b) shows a higher magnification TEM image of the Ni/Ti/MoTe<sub>2</sub>/Au/Ti/SiO<sub>2</sub> multilayered architecture of the active region. The contact between Au and MoTe<sub>2</sub> is not continuous and shows 5 nm to 20 nm wide voids distributed along the interface. Fig. S10 (c) shows a typical nano-beam diffraction (NBD) pattern of the MoTe<sub>2</sub> crystal in the Area 2. The pattern can be indexed as the [110] zone-axis of the 2H structure. No apparent differences could be recognized in all the areas by NBD mapping. Atomic resolution HAADF scanning transmission electron microscopy (STEM) was further employed to study the local defects of the MoTe<sub>2</sub> crystal in Area 2. Fig. S10 (d) shows a typical atomic image of the unperturbed 2H phase in most of the region in Area 2, representing a characteristic atomic structure of [110] zone-axis. At the MoTe<sub>2</sub>/Au interface, Te atoms connect closely with the Au atoms, ensuring low resistance contact formation for electrical measurements. Although no difference has been noticed by NBD analysis, a filament region was recognized in the MoTe<sub>2</sub> layer stack using atomic resolved HAADF-STEM analysis. Fig. S10(e,f) show high magnification atomic images of the distorted 2H<sub>d</sub> structure in the filament. As shown by the black circles, this 2H → 2H<sub>d</sub> distortion led to formation of a double layer Te structure from single Te layer in the original 2H phase. In addition, a relative shift of the MoTe<sub>2</sub> subunit cells can be identified by the round-dot and square-dot black lines, suggesting that the original atomic sites of the 2H structure were “shuffled” along the c-direction, thus, partially obscuring the van-der-Waals gap between the Te-Mo-Te tri-layers. It is difficult to understand precisely the nature of disorder in the 2H<sub>d</sub> structure from the STEM characterization. However, the NBD and STEM analyses suggest that the 2H<sub>d</sub> structure is a distorted modification of the 2H structure and is interpreted by us as a transient state toward the 1T' or T<sub>d</sub> phase.

After RESET, two structures were observed in the active region, a distorted 2H<sub>d</sub> state and the original 2H phase, which indicates that the RESET process only leads to a partial recovery (see Fig. S11).

#### Section S9: Model description of the transition from 2H to 2H<sub>d</sub>

While the 2H structure is based on the -AbA-BaB- stacking of hexagonal layers with MoTe<sub>6</sub> prismatic coordination, the stacking sequence in the 1T' and T<sub>d</sub> phases changes to -AbC-BcA- with octahedral coordination. Since 2H is a higher-symmetry structure (P6<sub>3</sub>/mmc) in comparison to 1T'/T<sub>d</sub>, its transformation into latter with preserved 2D-layers coherency should result in possible six variants of 1T'/T<sub>d</sub> that are related by nearly-60° rotation around the [001]<sub>2H</sub> axis. Our simulation of electron diffraction patterns in Fig. S12(a) shows that 2 out of 3 orientational variants of 1T'/T<sub>d</sub> have patterns similar to 2H in [110] zone-axis. One can indeed expect very similar electron diffraction patterns of 2H in [110] zone-axis (as well as its equivalent [100] and [010] zone-axes) and the 2-out-of-3 corresponding variants of 1T' (P2<sub>1</sub>/m, a = 0.633 nm, b = 0.3469 nm, c = 1.386 nm, α = 90 °, β = 93.92 °, γ = 90 °) and T<sub>d</sub> (Pmn2<sub>1</sub>, a = 0.3477 nm, b = 0.6335 nm, c = 1.3889 nm, α = 90 °, β = 90 °, γ = 90 °) phases. It would be difficult to

differentiate the three phases by analyzing the diffraction patterns in this particular orientation within the experimental error. However, 1T' and T<sub>d</sub> phases can be easily differentiated from 2H in appropriate crystallographic orientation. Fig. S12(b) shows that all the corresponding patterns of 1T' and T<sub>d</sub> phases produce additional reflections compared with that of 2H in [120] zone-axis, which means that in this particular orientation 1T' and T<sub>d</sub> phases can be differentiated from the 2H phase. As mentioned above (see Fig. 3(i, j) and Fig. S10(c)), no such additional reflections have been observed in the distorted 2H<sub>d</sub> region.

The STEM findings strongly suggest that the regions designated as 2H<sub>d</sub> are the filaments responsible for the LRS with the following structural characteristics: (1) 2H<sub>d</sub> is a structural derivative of 2H, as can be judged from the similarity of their reciprocal lattices, i.e. electron diffraction patterns, and from a correspondence of van-der-Waals gaps in both structures; (2) the identity of 2H and 2H<sub>d</sub> elemental compositions suggests that the 2H → 2H<sub>d</sub> transition is polymorphic, with structural changes due to local atomic displacements.

In order to understand the 2H<sub>d</sub> structure, we consider the possibility of its structural relation with the known polymorphs of 2H-MoTe<sub>2</sub>, i.e. 1T' and T<sub>d</sub> phases, which are both electrically conducting. In fact, T<sub>d</sub> phase inclusions have been observed in the 2H matrix (see Fig. 4(b)). Hereinafter, we corroborate that the 2H<sub>d</sub> filament is a *transient state* representing an incomplete process of switching from 2H to 1T' or T<sub>d</sub> phase structurally.

By a carefully analysis of the distorted atomic images of 2H<sub>d</sub>, we have constructed a P1 structure (see Fig. S13(a)) as a derivative of 2H with atomic displacements to match the major zone axes high-resolution images, e.g., in Fig. 3(f, h). This P1 structure also gives the diffraction patterns that match experimental NBDs in Fig. 3(i, j) (see Fig. S13(b)). Fig. S13(a) lists the crystallographic parameters of the P1 structure derived from matching HAADF images from 2H<sub>d</sub> regions. The structure represents a change of flat atomic layers of 2H to corrugated ones with a shift of atoms along the *c*-direction, but without changing the -AbA- stacking sequence. Analysis of the structural models of 1T', T<sub>d</sub> and P1 shows many similarities not only in diffraction patterns, but also in structural projections. With this proposed 2H → 2H<sub>d</sub> → 1T'/T<sub>d</sub> transition model in mind, we suggest that the 2H<sub>d</sub> filament is a *transient state* representing an incomplete process of switching from 2H to 1T'/T<sub>d</sub> phase structurally and electronically. Therefore, the distorted 2H<sub>d</sub> region can be interpreted as a *transient state*, with atoms displaced from 2H toward one of the lower symmetry structures, with the presence of local 1T'- or T<sub>d</sub>-type regions. With a sufficient fraction of such regions in the filament and their inter-connectivity, the electrically conductive pathways, comparable with characteristics of 1T' and T<sub>d</sub> phases, become possible.

#### Section S10: DFT modeling of 2H, 1T', and 2H<sub>d</sub> structures

To explore the energetics and relative stability of the 2H<sub>d</sub> transient state, ab initio calculations were conducted to evaluate total structural energies for fully relaxed 2H, 1T', and 2H<sub>d</sub> structures. The Vienna ab initio simulation program (VASP, version 5.4.4)<sup>9-12</sup> was used for all density-

functional theory (DFT) calculations, with projector augmented waves (PAW) and a generalized gradient approximation (GGA) for exchange energies. Electronic degrees of freedom were optimized with a conjugate gradient algorithm. Valence electron configurations were: Mo<sub>pv</sub>: 4p5s4d; Te: 5s<sup>2</sup>5p<sup>4</sup>. Van der Waals interactions were accounted for by the non-local correlation functional of Klimes et al.<sup>13</sup> An 800 eV cutoff-energy was used in the "high precision" option, which converges absolute energies to within a few meV per MoTe<sub>2</sub> formula-unit.

As it can be seen from Table S1, 2H is the ground-state for MoTe<sub>2</sub> in its bulk state, while the formation energies for 1T' and 2H<sub>d</sub><sup>relaxed</sup> structures are positive (where 2H<sub>d</sub><sup>relaxed</sup> is a product of relaxation from the 2H<sub>d</sub> state). Since we are focusing on a transient 2H to 1T' state, additional linear-response calculations were conducted to estimate the response of the 2H<sub>d</sub><sup>relaxed</sup> structure to energy perturbations. The calculations show that the 2H<sub>d</sub> structure is mechanically unstable and that its structural relaxation leads to a 2H<sub>d</sub><sup>relaxed</sup> state, which is very similar to 2H but of lower P $\bar{1}$  symmetry (see Fig. S14), as determined with the FINDSYM program<sup>14</sup>. Note that since the formation energy of 2H<sub>d</sub><sup>relaxed</sup> structure is within the DFT error from that of 2H, a clear conclusion about the stability of the 2H<sub>d</sub><sup>relaxed</sup> state cannot be drawn. Moreover, we notice that boundaries between different structures as observed in the experiment (see Figs. 3(d), 4(a) and (b)) that can be expected to drastically impact the energy landscape for the various structures in MoTe<sub>2</sub> are not captured in this DFT simulation. Thus, to unambiguously verify the observed 2H<sub>d</sub> structure theoretically, a comprehensive multiscale modeling that includes external fields, i.e., electrical, thermal and stress-related, will be beneficial to shed more light on the (meta)stability of the 2H<sub>d</sub> structure and reversibility of 2H  $\leftrightarrow$  2H<sub>d</sub> transition in MoTe<sub>2</sub> layers.

**Table S1.** DFT-calculated total energies and lattice parameters for fully relaxed 2H, 1T' and 2H<sub>d</sub> structures in the absence of electrical field

Structure	$\Delta U$ (eV per MoTe <sub>2</sub> formula), relative to 2H structure	Space group	Lattice constants (nm)
2H	0	P6 <sub>3</sub> /mmc	a=0.3573, b=0.3573, c=1.4268 $\alpha=90^\circ, \beta=90^\circ, \gamma=120^\circ$
1T'	0.029	P2 <sub>1</sub> /m	a=0.6402, b=0.3540, c=1.3964 $\alpha=90^\circ, \beta=93.74^\circ, \gamma=90^\circ$
2H <sub>d</sub> (input to DFT)	-	P1	a=0.7038, b=0.3519, c=1.3964 $\alpha=90^\circ, \beta=90^\circ, \gamma=120^\circ$
2H <sub>d</sub> <sup>relaxed</sup>	0.013	P $\bar{1}$	a=0.6223, b=0.3561, c=1.4499 $\alpha=89.99^\circ, \beta=89.02^\circ, \gamma=90^\circ$

### Section S11: LRS of MoTe<sub>2</sub> based RRAM devices

In our work, we observe a wide span of LRS values due to different compliance settings, scanning conditions, and different devices surface conditions. Fig. S15 is a zoom-in image of linear scale I-V curves of many vertical MoTe<sub>2</sub> RRAM devices. It is apparent that the LRS in the

black dotted measurement is much more linear than for other devices – this device was confirmed to be in its  $T_d$  phase using STEM.

#### Section S12: Temperature stability of $2H_d$ structure

In order to test the high temperature retention properties of the  $2H_d$  structure, devices were set to their LRS, and annealed and read at 400 K. An exemplary result is shown in Fig. S16 (a). 6 devices were monitored - none of them showed a change of resistance when annealed at 400 K for 24 h, indicating the  $2H_d$  structure is stable at 400 K. Next, these devices were annealed at 523 K (250 °C) (Fig. S16(b)), and re-measured at room temperature. After 8 h of annealing, 3 out of 6 devices dropped back to their HRS, which indicates that the  $2H_d$  is not stable at these elevated temperatures.

#### Section S13: $Al_2O_3/MoTe_2$ based RRAM

Fig. S17 shows I-V characteristics of a Ti/Au- $Al_2O_3$ -Ti/Ni stack.  $Al_2O_3$  is one of the early materials that was investigated for RRAM applications. However, for our film even repeated voltage sweeps did not result into any filament formation.  $Al_2O_3$  layers underwent a destructive breakdown at voltages in the 1.35 V range.

#### Section S14: C-AFM exploration of the switching mechanism in $MoTe_2$ RRAM

Since the top electrode in our RRAM design prevents a locally resolved scan of the currents through a  $MoTe_2$  flake after formation when employing a C-AFM (Veeco Dimension 3100 AFM) measurement, the top electrode had to be carefully removed prior to any further characterization. To do so, we used PMMA as etch mask to define the etching area and Nickel etchant TFB to etch away the top Ni contact and BOE to remove the Ti layer to access the TMD. We carefully checked that this etching approach did not harm the TMD and did not result in any additional features during the C-AFM measurements that would be unrelated to the forming process.

## References

1. Sangwan, V.K., *et al.* Gate-tunable memristive phenomena mediated by grain boundaries in single-layer MoS<sub>2</sub>. *Nature Nanotech.* **10**, 403-406 (2015).
2. Bessonov, A.A., *et al.* Layered memristive and memcapacitive switches for printable electronics. *Nature Mater.* **14**, 199-204 (2015).
3. Cheng, P., Sun, K. & Hu, Y.H. Memristive behavior and ideal memristor of 1T phase MoS<sub>2</sub> nanosheets. *Nano Lett.* **16**, 572-576 (2016).
4. Wang, M., *et al.* Robust memristors based on layered two-dimensional materials. *Nature Electronics* **1**, 130-136 (2018).
5. Ge, R., *et al.* Atomristor: Nonvolatile resistance switching in atomic sheets of transition metal dichalcogenides. *Nano Lett.* **18**, 434-441 (2018).
6. Hong, J., *et al.* Graphene as an atomically thin barrier to Cu diffusion into Si. *Nanoscale* **6**, 7503-7511 (2014).
7. Horcas, I., *et al.* WSXM: a software for scanning probe microscopy and a tool for nanotechnology. *Rev. Sci. Instrum.* **78**, 013705 (2007).
8. Appenzeller, J., Zhang, F., Das, S. & Knoch, J. Transition Metal Dichalcogenide Schottky Barrier Transistors: A Device Analysis and Material Comparison. in *2D Materials for Nanoelectronics* 207-240 (CRC Press, 2016).
9. Kresse G. and Hafner, J. Ab initio molecular dynamics for liquid metals. *Phys. Rev. B* **47**, 558 (1993).
10. Kresse, G. and Hafner, J. Ab initio molecular-dynamics simulation of the liquid-metal-amorphous-semiconductor transition in germanium. *Phys. Rev. B* **49**, 51 (1994).
11. Kresse, G. and Furthmüller, J. Efficiency of ab-initio total energy calculations for metals and semiconductors using a plane-wave basis set. *Comput. Mat. Sci.* **6**, 15 (1996).
12. Kresse, G. and Furthmüller, J. Efficient iterative schemes for ab initio total-energy calculations using a plane-wave basis set. *Phys. Rev. B* **54**, 11169 (1996).
13. Klimes, J., Bowler, D.A., and Michaelides, M., Van der Waals density functionals applied to solids, *Phys. Rev. B* **83** 195131 (2011).
14. Stokes, H.T. and Hatch, D.M. FINDSYM: Program for Identifying the Space Group Symmetry of a Crystal. *J. Appl. Cryst.* **38** 237 (2005); <http://stokes.byu.edu/iso/findsym.php>

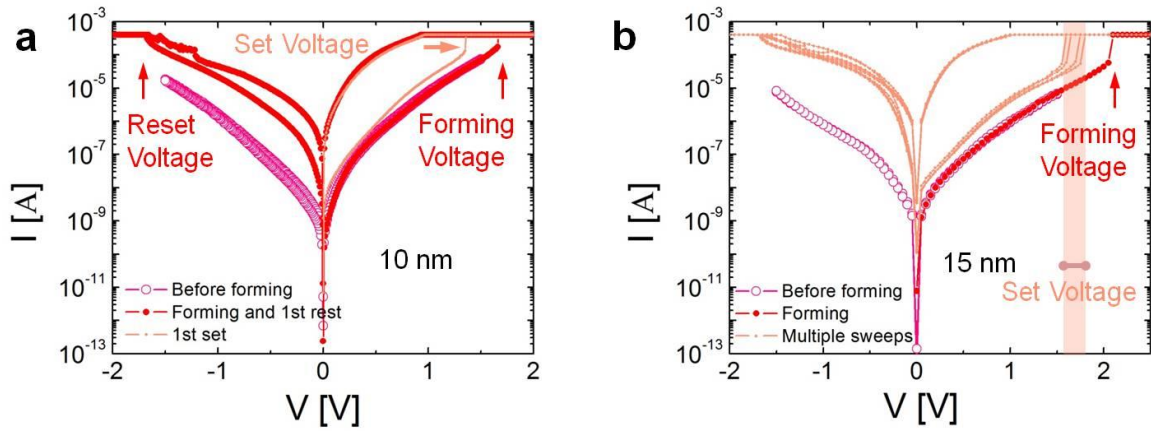


**Fig. S1. Typical I-V curves of a vertical MoTe<sub>2</sub> RRAM showing the forming process. (a)** RRAM forming for a 10 nm thick flake including first set and reset. **(b)** Multiple sweeps after forming had occurred for a 15 nm flake. Note the rather narrow “band” of set voltages. Current compliance is set to 400  $\mu$ A for both cases.

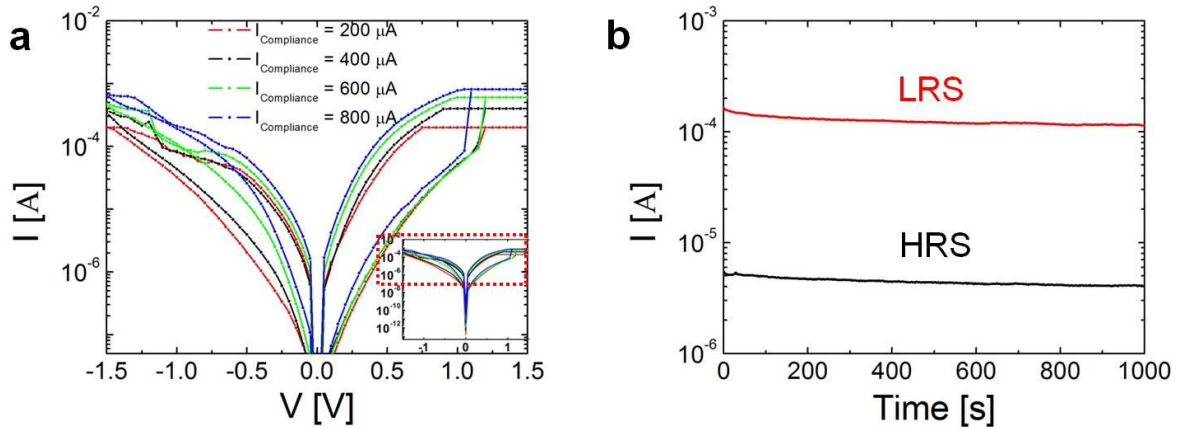


**Fig. S2. Current compliance setting effect on RRAM performance and its stability. (a)** DC switching characteristic for a 7 nm thick MoTe<sub>2</sub> flake for different current compliances. **(b)** shows read disturb measurements for the same RRAM device at 0.5 V with the current compliance set to 800  $\mu$ A.

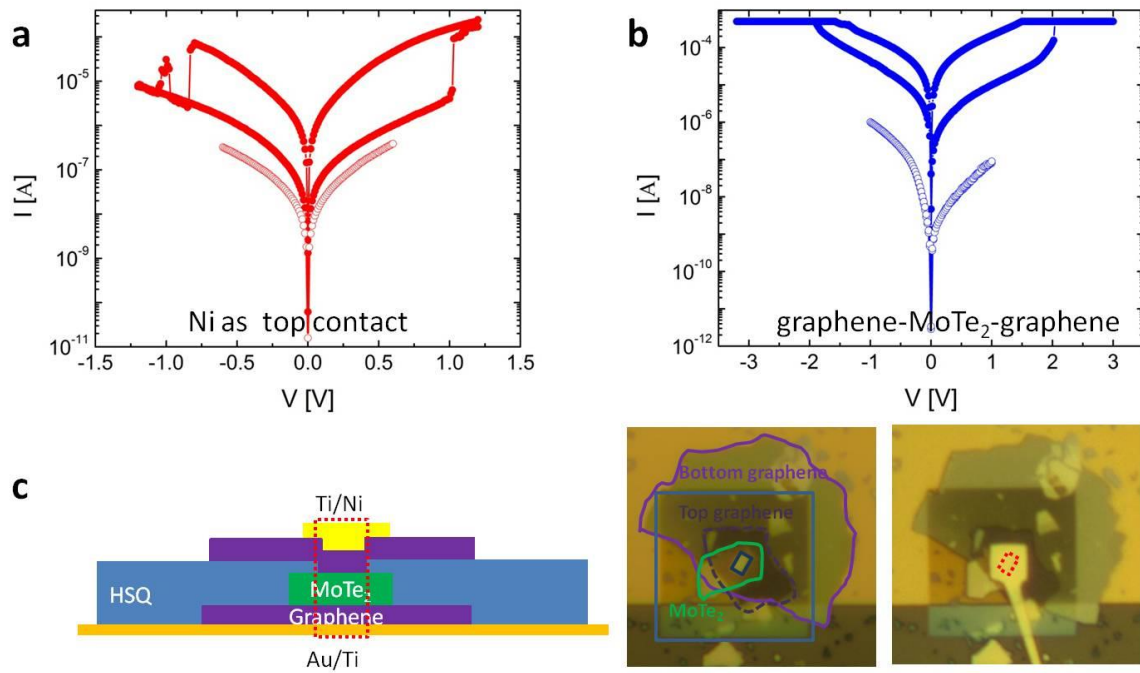


**Fig. S3. Impact of the choice of metal electrodes on the RRAM behavior.** (a) The intrinsic and RRAM curves of a vertical MoTe<sub>2</sub> device with Ni as top contact. The Au bottom pad is the source in these measurements. (b) The intrinsic and RRAM curves of a vertical graphene-MoTe<sub>2</sub>-graphene device. The top graphene layer acts as the source in these measurements. (c) A schematic and optical images of a graphene-MoTe<sub>2</sub>-graphene device. Note that the bottom graphene is located on a Au pad and that the top graphene layer is capped by a Ti/Ni electrode to ensure true vertical transport.

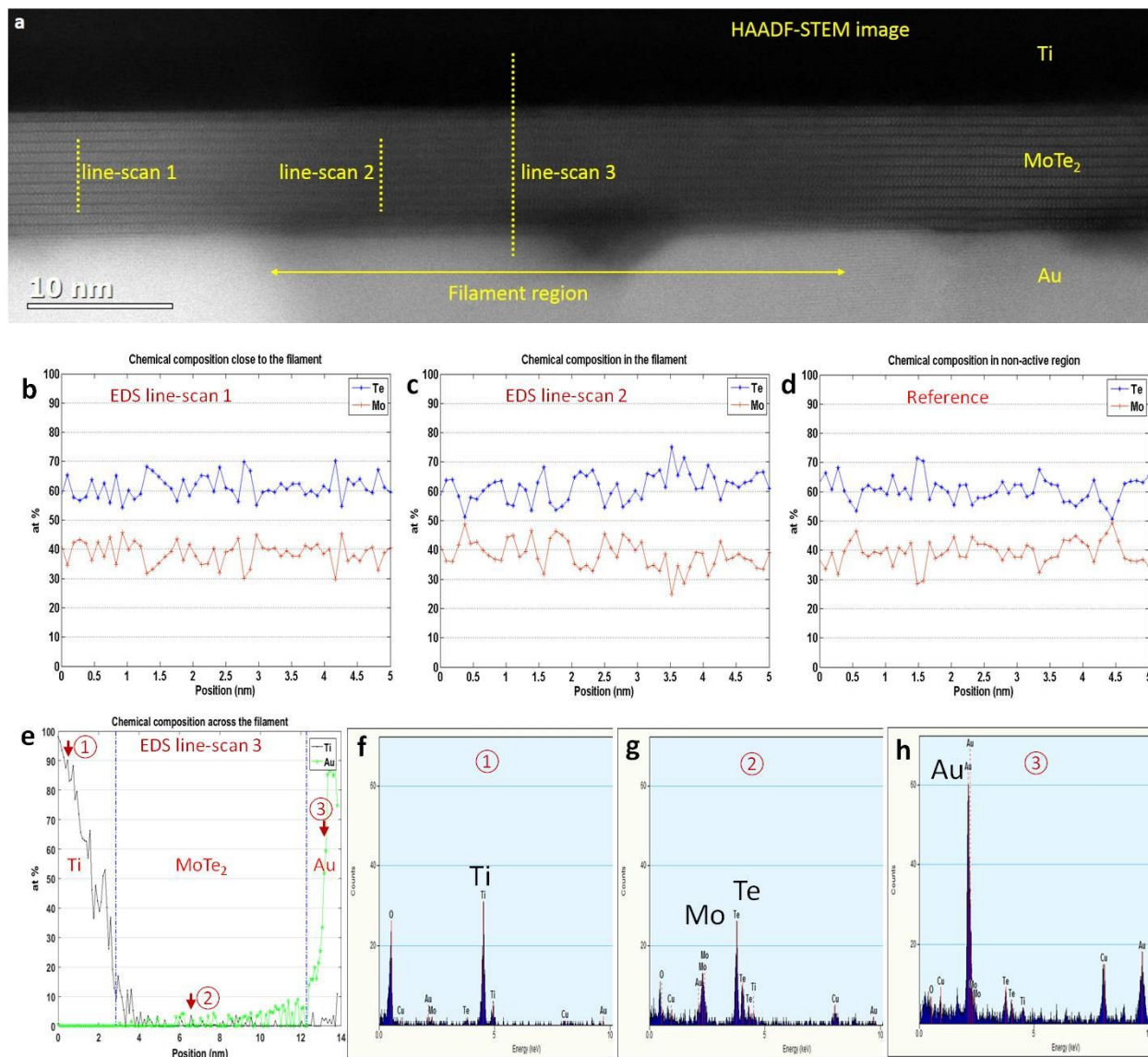


**Fig. S4. EDS line-scan analysis on a device in its low resistive state (LRS) after repeatedly cycling the device from the HRS to the LRS.** (a) HAADF-STEM image showing a filament and the line-scan positions in an active region. (b) Line-scan close to the filament. (c) Line-scan in the filament. (d) Reference line-scan from a non-active region. (e) Line-scan across the filament showing no evidence of Ti or Au presence in the MoTe<sub>2</sub> layer. Blue lines showing the interfaces of the Ti/MoTe<sub>2</sub> and MoTe<sub>2</sub>/Au layers. The red arrows and numbers indicate the positions where individual single pixel raw EDS spectra were extracted for figures (f-h), respectively.

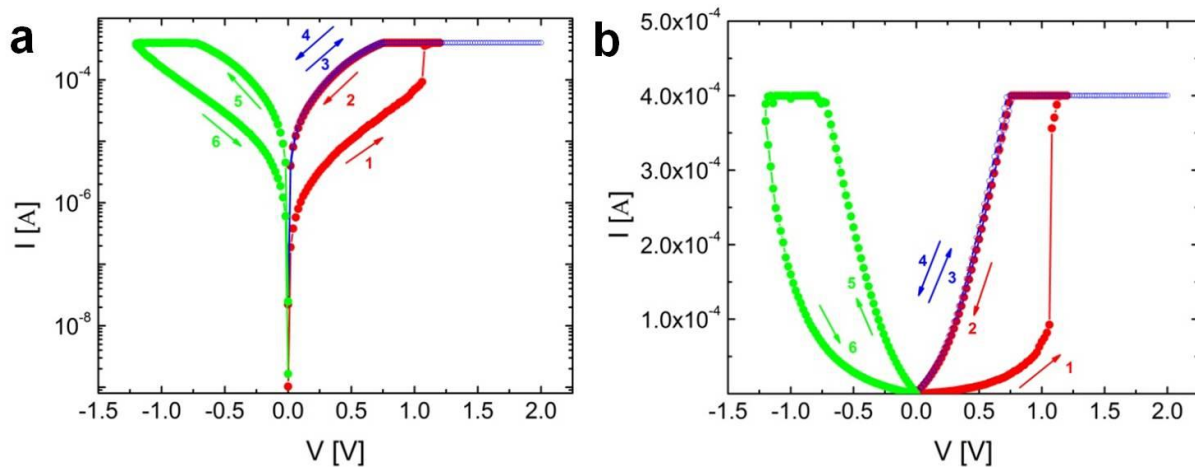


**Fig. S5. Bipolar RRAM behavior in MoTe<sub>2</sub> devices.** Multiple scans on a MoTe<sub>2</sub> based RRAM device plotted (a) on a logarithmic and (b) on a linear scale.

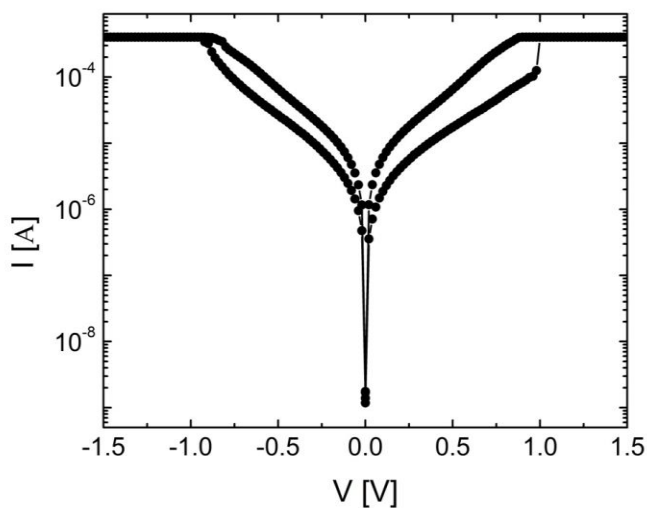


**Fig. S6. I-V curve of a 8 nm MoTe<sub>2</sub> device with a set voltage of  $1.0 \pm 0.1$  V.**

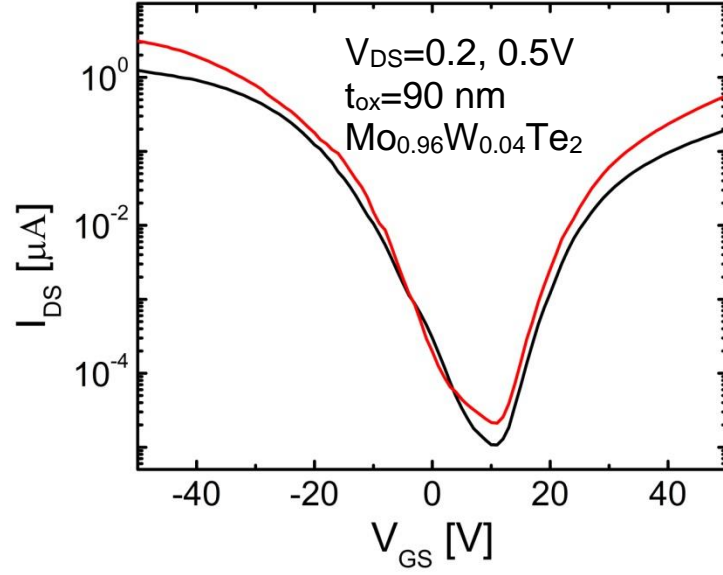
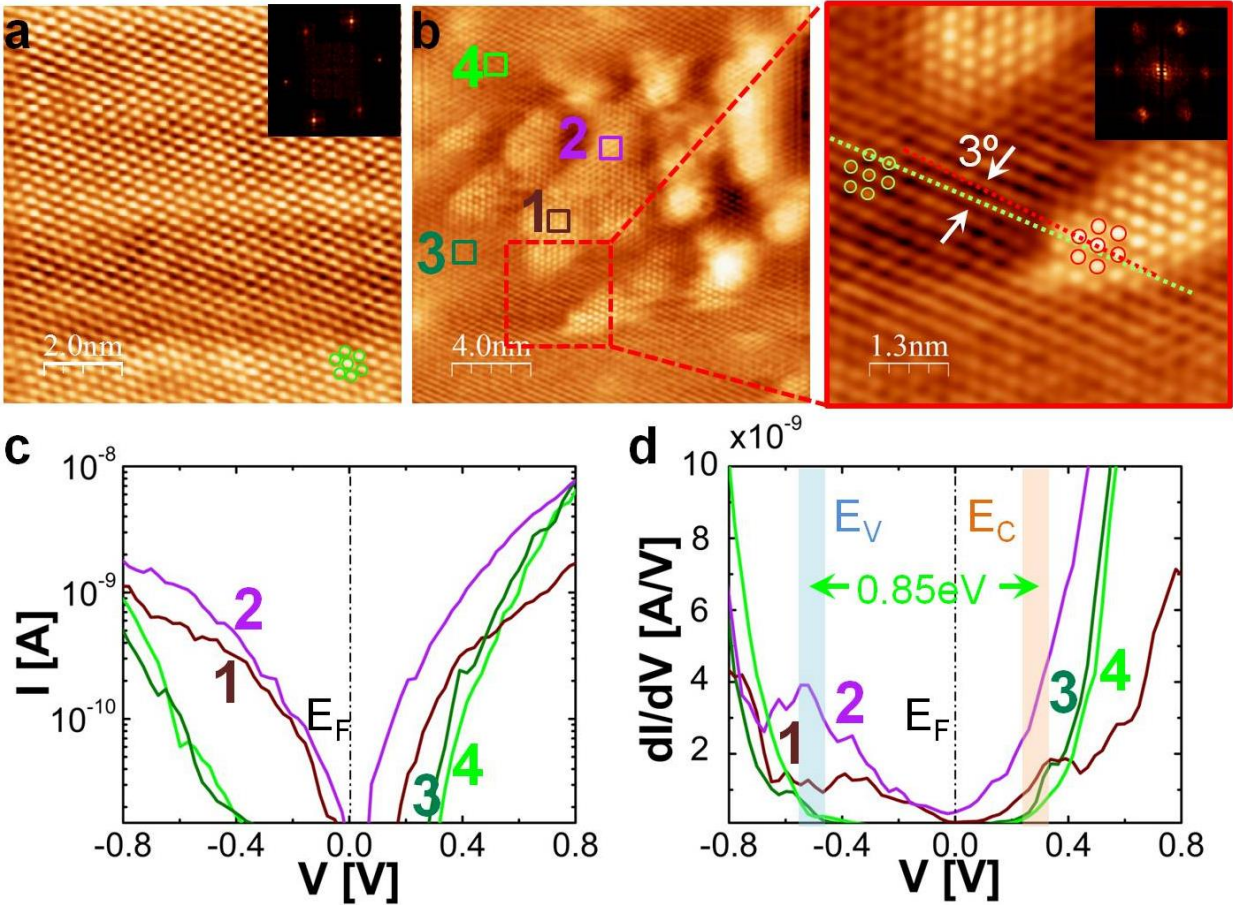
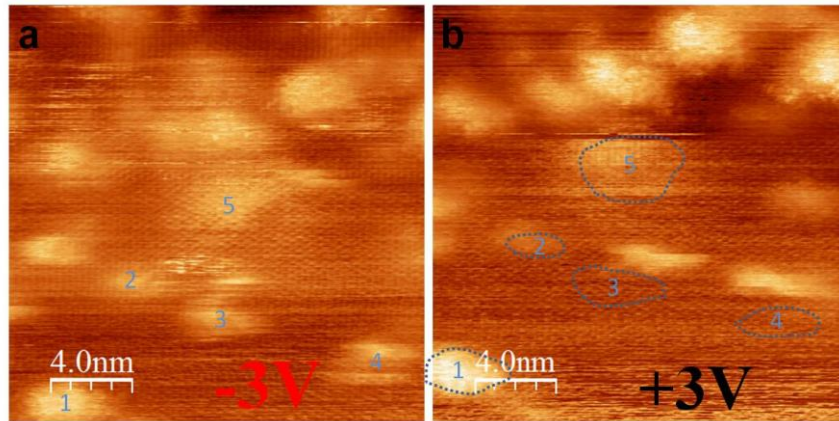


Fig. S7. Transfer characteristic of a  $\text{Mo}_{0.96}\text{W}_{0.04}\text{Te}_2$  back-gated device.



**Fig. S8. STM and STS analysis.** (a) STM image (filtered) of the pristine MoTe<sub>2</sub> surface. (b) STM image (filtered) of a portion of the surface region in (a) after a voltage of -3 V was applied to a contact underneath the TMD relative to the STM tip. The zoom-in image indicates that the position of Te atoms has changed after voltage application. The Te rows in the voltage modified region are rotated  $\sim 3^\circ$  relative to the atomic rows in the pristine part. However, the  $C_3$  symmetry of the atomic lattice is still clearly visible (green circles for pristine part and red circles for modified area). All images were recorded at tunneling currents of 2 nA and a bias voltage of -0.9 V. (c) shows I-V characteristics obtained by STS measurements corresponding to locations 1 through 4 in (b). (d) shows the corresponding dI/dV spectra with the blue band indicating the position of the valance band edge and the orange band indicating the position of the conduction band edge for the pristine MoTe<sub>2</sub> in agreement with the I-V characteristics of locations 3 and 4. Note that 1 and 2 suggest the absence of a bandgap (or existence of a very small gap) after voltage application.



**Fig. S9. STM analysis with different voltage polarity.** (a) STM image of a MoTe<sub>2</sub> surface after applying -3V. (b) STM image of the same MoTe<sub>2</sub> surface in (a) after +3V scanning.

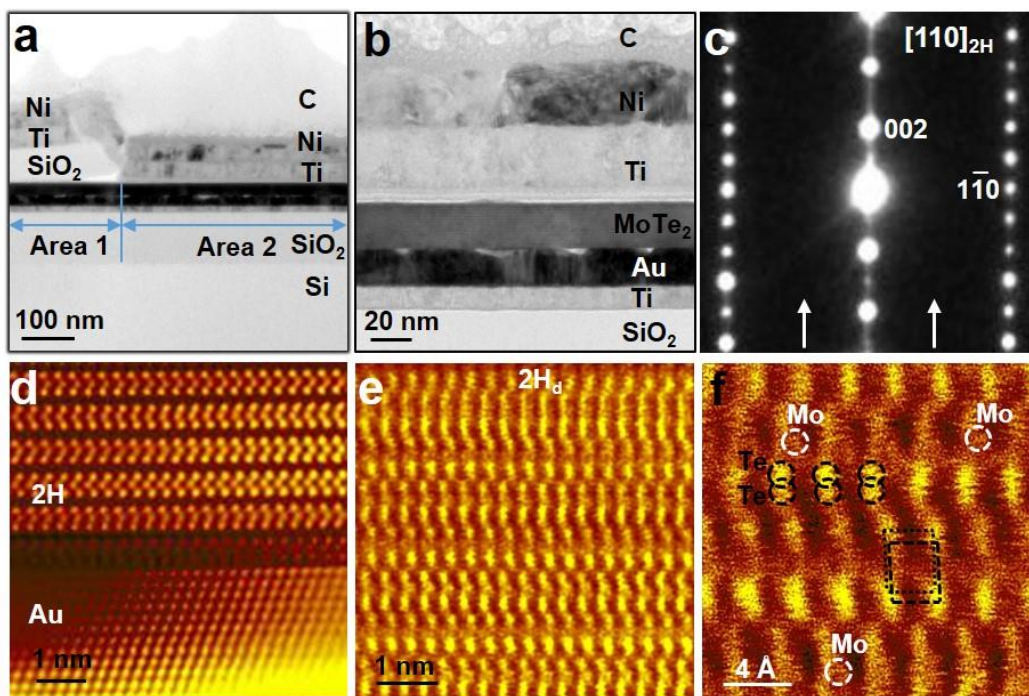


**Fig. S10. STEM measurement and analysis on MoTe<sub>2</sub> device.** (a) Bright-field TEM image showing the cross-section of a MoTe<sub>2</sub> device with ‘Area 1’ denoting the electrically non-active region and ‘Area 2’ denoting the electrically cycled active region. (b, d, e, f) images were taken from Area 2. (c) Nano-beam diffraction pattern taken along the [110]<sub>2H</sub> zone-axis from (e,f) area. (d) Atomic resolution HAADF image showing the typical undisturbed 2H structure of the MoTe<sub>2</sub> crystal along the [110]<sub>2H</sub> zone-axis, also showing the atomic contact at the interface of MoTe<sub>2</sub> and the bottom Au-electrode. (e, f) HAADF images showing the details of the distorted 2H<sub>d</sub> structure. Black and white circles denote the recognizable Te-sites and Mo-sites respectively. Black round dot and square dot lines illustrating the atomic shift in the neighboring layers along the view direction.

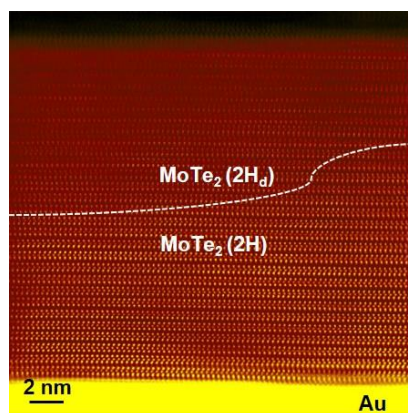


**Fig. S11. HAADF image shows a distorted structure (2H<sub>d</sub>) and 2H phase in the filament for a MoTe<sub>2</sub> device in HRS.**

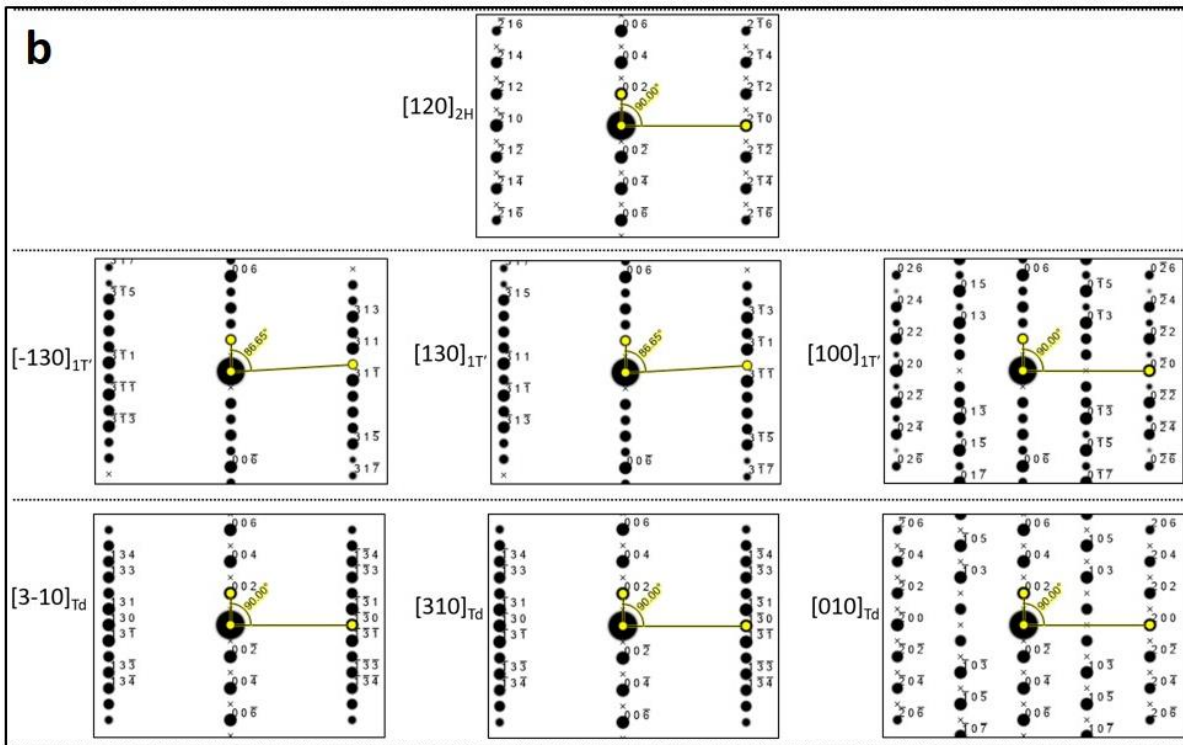
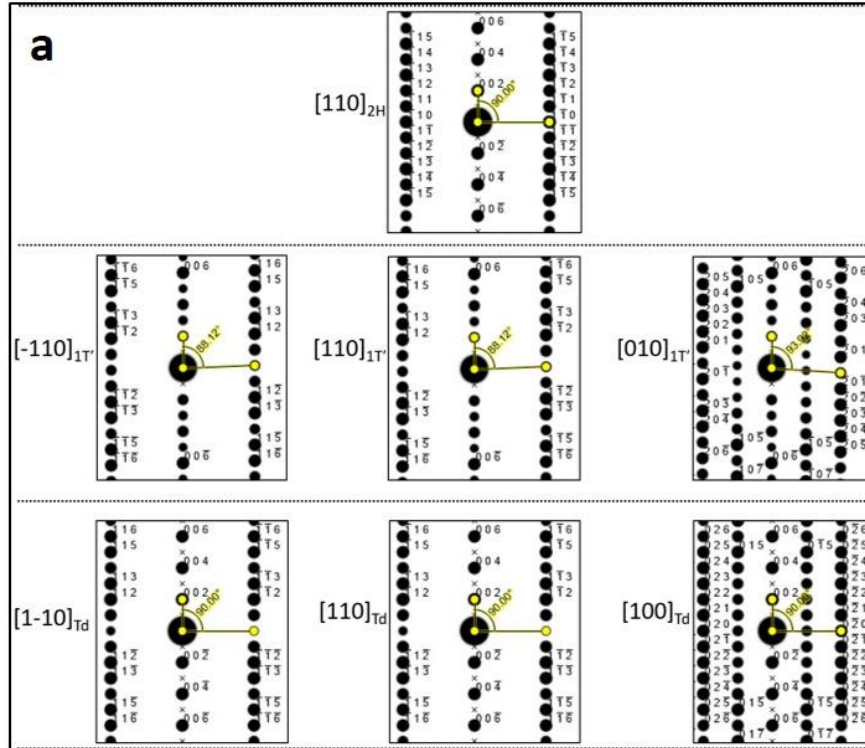


**Fig. S12. Simulated electron diffraction patterns of 2H, 1T' and Ta phases.** Simulated electron diffraction patterns of 2H phase in (a) [110] zone-axis and (b) [120] zone-axis, together with the patterns of their corresponding variants of 1T' and T<sub>d</sub> phases. Note that 2-out-of-3

patterns of the variants of 1T' and T<sub>d</sub> depicted in (a) show similarity with that of 2H in [110] zone-axis, unlike the [120] zone-axis case depicted in (b).

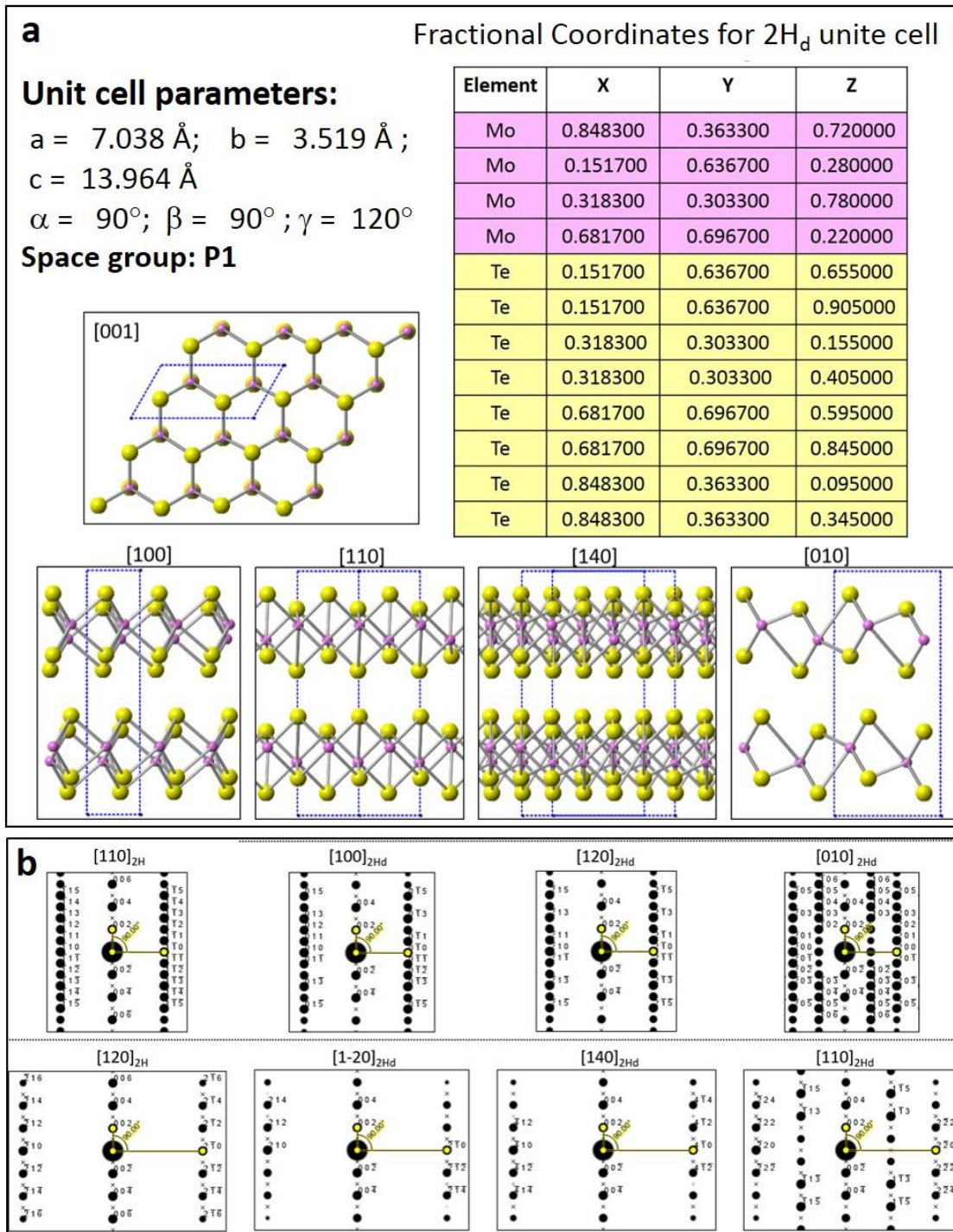


**Fig. S13. P1 model.** (a) Crystallographic parameters of the proposed 2H<sub>d</sub> structure derived from matching HAADF images from 2H<sub>d</sub> regions, together with detailed projection of the atomic model. The structure represents a change of flat atomic layers of 2H to corrugated, with shift of

atoms along the  $c$ -direction, but without changing the -AbA- stacking sequence. **(b)** Simulated diffraction patterns showing 2/3 of the variants of  $2H_d$  have similar patterns as that of  $2H$  both in  $[110]_{2H}$  and  $[120]_{2H}$  zone-axes.

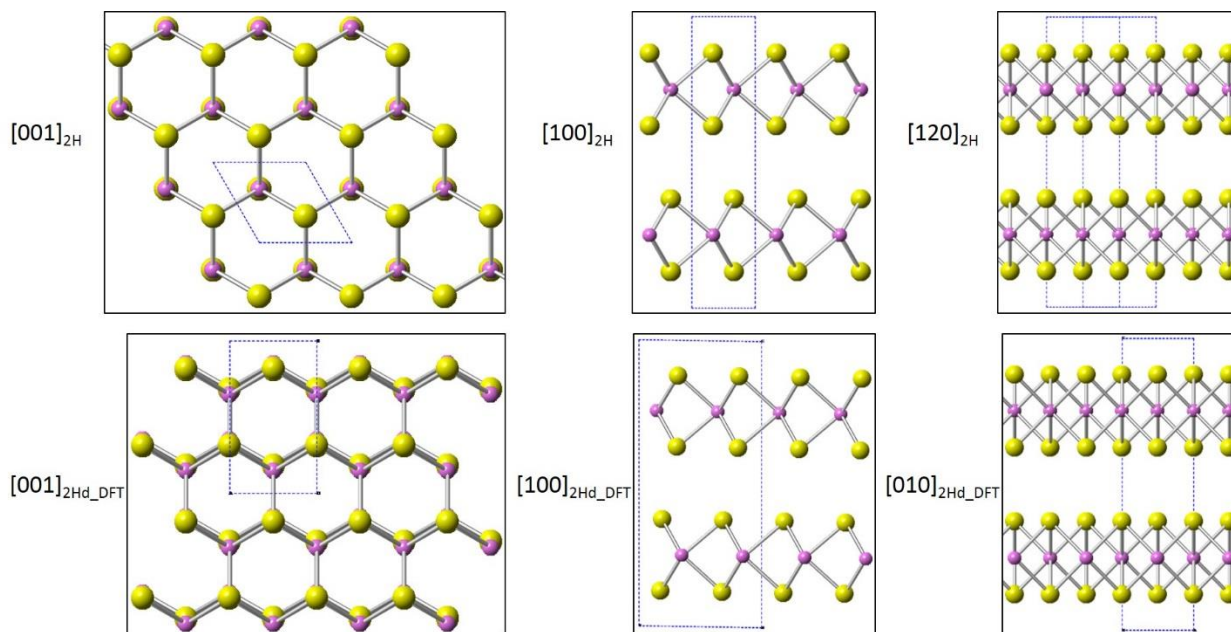


**Fig. S14. Comparison of the projections of the atomic models of  $2H$  and relaxed  $2H_d$  structure calculated by DFT.** The corresponding top-views and side-views show that the relaxed  $2H_d$  structure is very similar to  $2H$  structure.

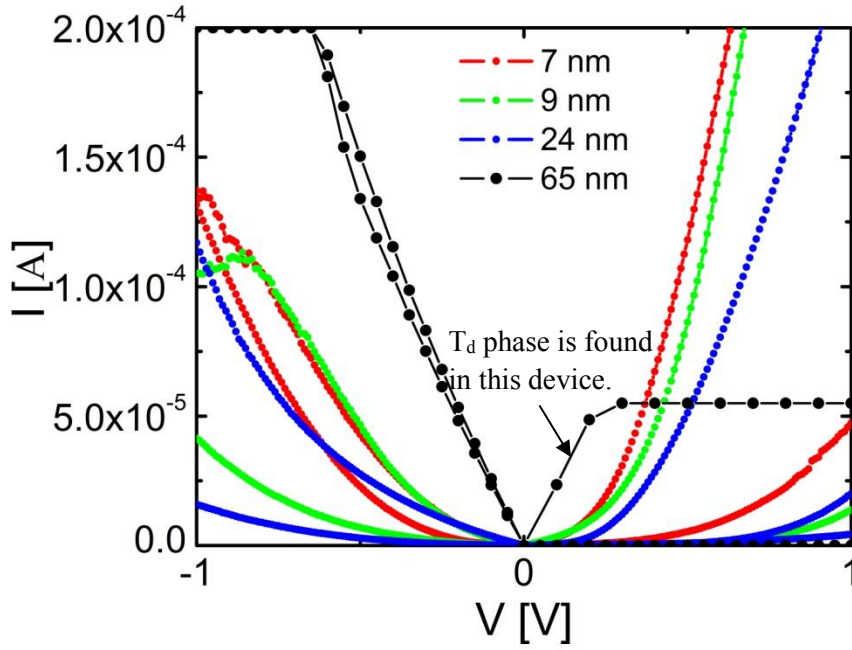


**Fig. S15. Linear scale I-V curves of vertical MoTe<sub>2</sub> RRAM devices after forming.**

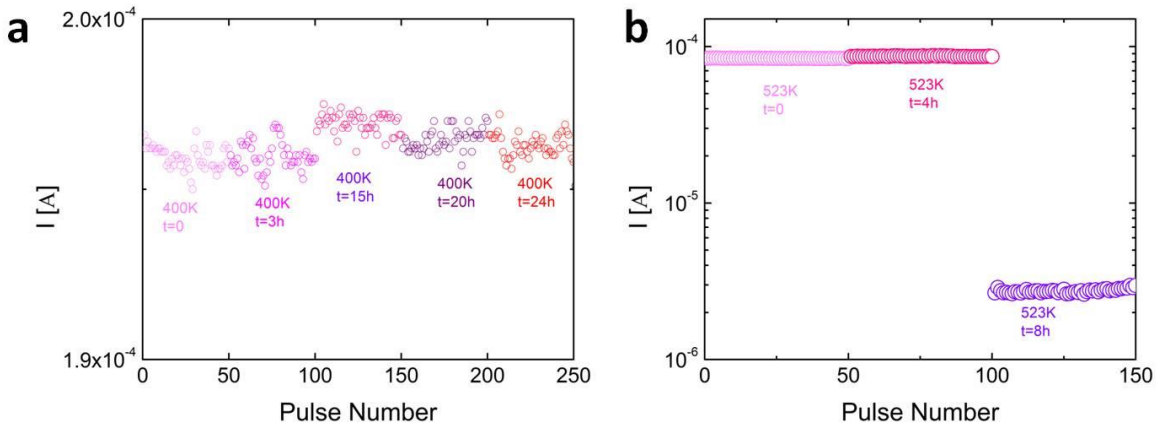


**Fig. S16. Temperature stability of the LRS.** (a) Read pulse test for one exemplary MoTe<sub>2</sub> based RRAM device annealed at 400K for 24h. (b) Read pulse test for one exemplary MoTe<sub>2</sub> based RRAM device annealed at 523K. The LRS (2H<sub>d</sub> structure) for this particular device changed back into its HRS (2H phase) after 8h.

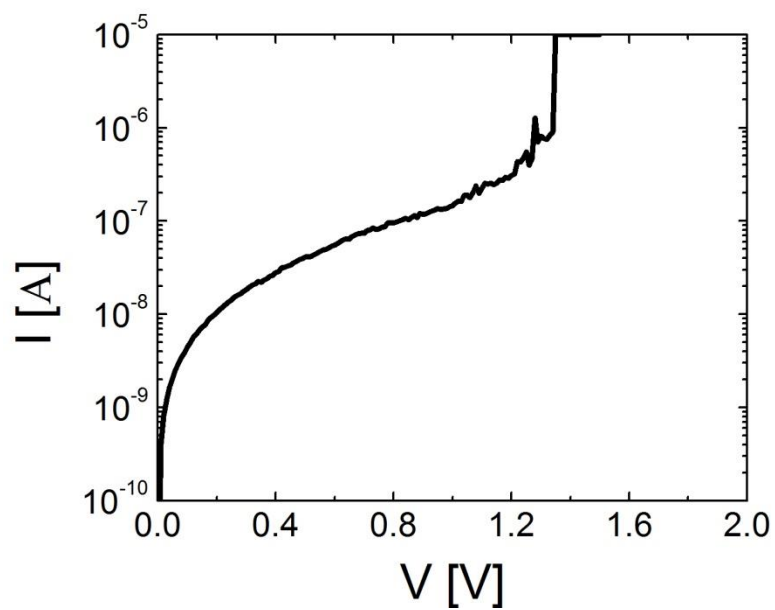


**Fig. S17. I-V curve of a metal- $\text{Al}_2\text{O}_3$ -metal device with an area of 330nm x 400nm.** Note that the  $\text{Al}_2\text{O}_3$  film breaks down at about 1.35 V.